



UNIVERSIDAD DE INVESTIGACIÓN DE TECNOLOGÍA EXPERIMENTAL YACHAY

Escuela de Ciencias Físicas y Nanotecnología

TÍTULO: Nano-engineered Cement

Trabajo de integración curricular presentado como requisito para la
obtención del título de Ingeniero en Nanotecnología

Autor:

Pizha Lema José David

Tutor:

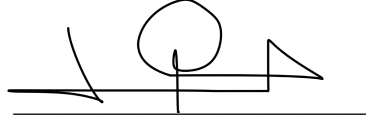
Dr.rer.nat. Julio C. Chacón-Torres (PhD.)

Urcuquí, Junio 2024

AUTORÍA

Yo, **PIZHA LEMA JOSE DAVID**, con cédula de identidad 0301524153, declaro que las ideas, juicios, valoraciones, interpretaciones, consultas bibliográficas, definiciones y conceptualizaciones expuestas en el presente trabajo; así como, los procedimientos y herramientas utilizadas en la investigación, son de absoluta responsabilidad de el/la autora (a) del trabajo de integración curricular. Así mismo, me acojo a los reglamentos internos de la Universidad de Investigación de Tecnología Experimental Yachay.

Urcuquí, Junio 2024.

A handwritten signature in black ink, consisting of a circle above a horizontal line with a vertical stem and a small triangle on the right side.

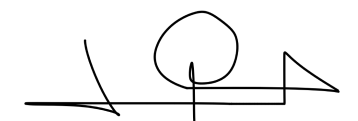
José David Pizha Lema
CI: 0301524153

AUTORIZACIÓN DE PUBLICACIÓN

Yo, **PIZHA LEMA JOSE DAVID**, con cédula de identidad , cedo a la Universidad de Investigación de Tecnología Experimental Yachay, los derechos de publicación de la presente obra, sin que deba haber un reconocimiento económico por este concepto. Declaro además que el texto del presente trabajo de titulación no podrá ser cedido a ninguna empresa editorial para su publicación u otros fines, sin contar previamente con la autorización escrita de la Universidad.

Asimismo, autorizo a la Universidad que realice la digitalización y publicación de este trabajo de integración curricular en el repositorio virtual, de conformidad a lo dispuesto en el Art. 144 de la Ley Orgánica de Educación Superior.

Urcuquí, Junio 2024.

A handwritten signature in black ink, consisting of a series of loops and lines, positioned above a horizontal line.

José David Pizha Lema
CI: 0301524153

Dedication

To grandma

José D. Pizha

Acknowledgements

I am deeply grateful to everyone who has supported me along this journey, from the dedicated cleaning staff to the esteemed professors who form the foundation of Yachay Tech University.

First and foremost, I want to express my heartfelt gratitude to those who made this work possible. I am indebted to my advisor, Prof. Dr. Julio Chacón, for his invaluable guidance and patient mentorship. Additionally, I extend my thanks to the dedicated staff of the Nanotechnology department, specifically to Johanna Pilicita for her remarkable organizational skills, which ensured the smooth execution of experiments, to Darwin Méndez for his ingenuity in assembling molds and adapting features to the universal testing machine, and to Prof. Dr. Gema González for her meticulous manuscript revision and correction. Lastly, I would like to thank Prof. Dr. Carlos Loyo for facilitating mechanical test measurements and manuscript revisions.

Equally, I am thankful for the unwavering support and camaraderie of my fellow graduate students, especially Antonella Macias and Josue Delgado, as well as dear friends Guido Tapia, Marcial Valero, and Mateo Carpio. Their presence on campus has made this journey truly rewarding and memorable.

I want to specially express my deepest thanks to my parents, Maria Lema and David Pizha, as well as my sister, Dr. Ines Pizha. Their unwavering support and belief in me have been a constant source of strength and inspiration.

Lastly, but certainly not least, I would like to thank some special individuals: Ing. Ruben Lema, Ing. José Guaman, Ing. Juan Guaman, and Dr. Priscilla Quezada. Thank you for your friendship.

José D. Pizha

Resumen

El hormigón es ampliamente utilizado en la industria de la construcción debido a su rendimiento deseable, la accesibilidad de sus ingredientes y su bajo costo. Sin embargo, se caracteriza por ser un material quasi-frágil, exhibiendo baja resistencia a la tracción y escasa capacidad de deformación, lo que lo hace más susceptible a grietas y reduce su durabilidad. Con el objetivo de abordar este problema, se han incorporado fibras, tanto micro como macro (polipropileno, nailon, polietileno y barras de acero.), al concreto, creando así un material compuesto con mejoras en su rendimiento tanto en tensión como en compresión. A pesar de estas mejoras, las fibras solo logran retrasar el desarrollo de microfisuras y no evitan su inicio a escala nanométrica. Por lo tanto, ha surgido un creciente interés en fusionar las propiedades intrínsecas de las nanoestructuras basadas en carbono (CNS) en la matriz del cemento, dando lugar al desarrollo de cemento nano-modificado (nanocemento). Los materiales modificados a escala nanométrica han demostrado mejoras significativas en sus propiedades mecánicas, eléctricas y térmicas en comparación con sus homólogos a mayor escala. Sin embargo, una de las principales dificultades en la síntesis del nanocemento radica en lograr una dispersión homogénea de las CNS en la matriz hidráulica del cemento. Los CNS, debido a su hibridación estable sp^2 , son químicamente inertes e incompatibles con muchos disolventes, lo que dificulta alcanzar una dispersión uniforme. En este trabajo, nuestro objetivo es producir cemento mediante nanoingeniería incorporando directamente CNS en la matriz del cemento a través de dos enfoques: in situ mediante deposición química de vapor (CVD) o utilizando un molino de bolas. En el primer experimento, se crea un compuesto de grafeno/cemento cultivando grafeno directamente en la matriz de cemento mediante CVD. En el segundo experimento, se produce grafeno mediante CVD y luego se muele con cemento para inducir la funcionalización mecánica. Las propiedades estructurales, morfológicas e interacciones superficiales del nanocemento se analizan mediante diversas técnicas analíticas, que incluyen espectroscopia Raman, difracción de rayos X en polvo (XRD), espectroscopia fotoelectrónica de rayos X (XPS), microscopía electrónica de barrido (SEM), análisis termogravimétrico (TGA) y pruebas mecánicas realizadas con una máquina de ensayo universal (UTM). El objetivo principal de este análisis es evaluar la eficacia en la preparación del compuesto de cemento nano-modificado.

Palabras clave: Cemento nano-modificado, nanocompuesto, grafeno/cemento, CNT/cemento

Abstract

Concrete is one of the most commonly used materials in the construction industry due to its desirable performance, easily accessible ingredients, and low cost. However, it is typically characterized as a quasi-brittle material with low tensile strength and low strain capacity, making it more susceptible to cracks and poor durability. To address this challenge, micro and macro fibers (e.g., polypropylene, nylon, polyethylene, and steel bars) have been incorporated into concrete to create a composite material that exhibits improved performance in both tension and compression modes. Despite these enhancements, fibers can only delay the development of microcracks and do not prevent their initiation at the nano scale. Therefore, there is growing interest in merging the intrinsic properties of carbon-based nanostructures (CNS) into the cement matrix, leading to the development of nano-engineered cement. Nano-engineered materials have demonstrated significant improvements in their mechanical, electrical, and thermal properties compared to their counterparts at larger scales. However, one of the main difficulties in the synthesis of nanocement is the homogeneous dispersion of the CNS into the cement polymeric matrix. CNS, due to their stable sp^2 hybridization, are chemically inert and incompatible with many solvents, making it challenging to achieve a uniform dispersion. In this work, our aim is to produce nano-engineered cement by directly incorporating CNS into the cement matrix through two approaches: in-situ *via* chemical vapor deposition (CVD) or ball milling. A graphene/cement composite is created by growing graphene directly into the cement matrix via CVD. In a second experiment, graphene is first produced by CVD and then milled with cement to induce mechanical functionalization. The structural analysis, surface morphology, and surface interactions of the nanocement are characterized using Raman spectroscopy, X-ray powder diffraction (XRD), X-ray photoelectron spectroscopy (XPS), scanning electron microscopy (SEM), thermogravimetric analysis (TGA), and a universal testing machine (UTM) to evaluate the efficiency in the preparation of a nano-engineered cement composite.

Keywords: Nano-engineered cement, nanocomposite, graphene/cement, CNT/cement

Contents

List of Figures	xii
List of Tables	xiv
Abbreviations	xvii
1 Introduction	1
2 Theoretical Background	3
2.1 Nanotechnology	3
2.2 Carbon allotropes	4
2.3 Graphene	4
2.3.1 Graphene electronic structures	5
2.3.2 Graphene mechanical properties	6
2.3.3 Graphene synthesis	7
2.4 Carbon nanotubes	8
2.4.1 CNT electronic Structure	9
2.4.2 CNT mechanical properties	11
2.4.3 CNT synthesis	11
2.5 Portland cement	13
2.5.1 Mineral composition of Portland cement	13
2.5.2 The hydration of Portland cement	14
2.6 Nanocomposites	16
2.6.1 Carbon based nanostructured cement	17
2.7 Characterization techniques	19
2.7.1 Raman spectroscopy	19
2.7.2 Raman spectroscopy of Carbon allotropes	20
2.7.3 X-Ray Diffraction (XRD)	23
2.7.4 X-Ray Photoelectron Spectroscopy (XPS)	24

2.7.5	Scanning X-ray induced secondary electron images (SXISE)	25
2.7.6	Thermogravimetric analysis (TGA)	25
3	Motivation	27
3.1	Problem Statement	27
3.2	General and Specific Objectives	28
3.2.1	General Objectives	28
3.2.2	Specific Objectives	28
4	Methodology	29
4.1	Materials and Equipment	29
4.1.1	Materials	29
4.1.2	Equipment	29
4.2	Synthesis of glucose-derived nanostructure	30
4.3	Synthesis of nano-engineered cement	31
4.4	Specimen preparation	32
4.5	Characterization	34
5	Results & Discussion	37
5.1	Glucose based nanostructures	37
5.1.1	Raman spectroscopy and XRD	37
5.2	Nano-engineered cement	39
5.2.1	Raman	39
5.2.2	XRD	42
5.2.3	TGA	44
5.2.4	XPS	46
5.2.5	Mechanical test	47
5.2.6	SXISE	49
5.2.7	Water immersion test	53
6	Conclusions & Outlook	55
	Bibliography	57

List of Figures

2.1	Carbon allotropes	5
2.2	Electronic properties of graphene	6
2.3	Synthesis methods of graphene	8
2.4	Electronic Structure of CNT	9
2.5	Synthesis of CNT	12
2.6	Cement production diagram	13
2.7	Potential applications of nano-engineered cement	18
2.8	Raman spectroscopy working principal	20
2.9	Raman spectroscopy graphene	21
2.10	Raman spectroscopy of SWCNT and MWCNT	22
2.11	X-Ray Diffraction working principal	23
2.12	X-Ray Photoelectron Spectroscopy working principal	24
2.13	Thermogravimetric analysis working principal	26
4.1	Equipment's used for the synthesis of nano-engineered cement and specimen preparation	30
4.2	Synthesis methods of multi-layer graphene	31
4.3	Synthesis methods of nano-engineered cement	32
4.4	Specimen preparation	33
4.5	Characterization equipments	35
5.1	Glucose materials	38
5.2	Synthesis of nano-engineered cement <i>via</i> CVD.	40
5.3	Synthesis of nano-engineered cement through Ball milling	41
5.4	XRD of plain cement and its phases	42
5.5	XRD patterns of cement and nano-engineered cement synthesized: <i>via</i> CVD, and through ball milling.	43
5.6	TGA curve of plain cement	45
5.7	Cement and byproducts	45
5.8	XPS patterns of cement and nano-engineered cement synthesized: <i>via</i> CVD, and through ball milling.	46
5.9	Compressive modulus and flexural strength	48

5.10 SXISE image of pain mortar	50
5.11 SXISE image of mortar produced with nano-engineered cement (CNT(YT)/CG)	51
5.12 SXISE image of mortar produced with nano-engineered cement (MLG/CG)	52
5.13 Water immersion test	53

List of Tables

2.1	Mechanical Properties of Materials	11
2.2	Nomenclature of cement components	14
2.3	Different types of nanocomposites	17
4.1	Summary of products	33
5.1	Mechanical Test Results	47

Abbreviations

- C-S-H** Calcium silicate hydrates 15
CG Cement Guapan 29
CNS Carbon nanostructure 1
CNT Carbon nanotube 1
CNT(NC) NC3100™ Research grades - Thin MWCNT 95+%C purity 29
CNT(YT) Multi-walled Carbon nanotube produced at Yachay Tech University 29
CT Calcination treatment 31
CVD Chemical vapor deposition 2
- FWHM** Full width at half maximum 37
- ICSD** Inorganic Crystal Structure Database 39
- MLG** Multi-layer graphene 31
MWCNT Multi-walled carbon nanotubes 8
- RBM** Radial breathing mode 22
- SEM** Scanning electron microscopy 25
SWCNT Single-walled carbon nanotubes 8
SXISE scanning X-ray induced secondary electron images 25
- TG** thermogravimetry 26
TGA Thermogravimetric analysis 25
- UTM** Universal Test Machine 34
- VdW** Van der Waals 2
- XPS** X-ray photoelectron spectroscopy 24
XRD X-ray diffraction 23

Chapter 1

Introduction

We are in the midst of a new industrial revolution driven by the application of quantum physics, which has facilitated a remarkable advancement in scientific and technological progress at the nanoscale. Materials modified at the nanoscale exhibit enhanced mechanical, electrical, and thermal properties compared to those at micro and macro scales¹. These properties have enabled the creation of innovative smart materials tailored to meet modern requirements and challenges.

In the realm of civil engineering, cement concrete stands as a cornerstone due to its affordability and durability². The global production of cement surpassed 4 billion tons in 2020, driven primarily by rapid population growth and infrastructure development in nations like China and India. With increasing global urbanization and infrastructure projects on the horizon, the demand for cement concrete is expected to escalate³.

Despite its significant compressive strength and durability, cement exhibits an intrinsic quasi-brittle nature characterized by low tensile strength and limited fracture propagation ability. Efforts to address these limitations have involved the incorporation of admixtures and fibers, particularly macrofibers and microfibers, to reinforce cementitious materials³. However, while microfibers can mitigate the progression of microcracks, they are ineffective at preventing their initial development at the nanoscale⁴.

Another pressing concern within the cement industry is the release of carbon dioxide (CO_2) during the manufacturing process. In 2019, global cement output reached approximately 4.5 billion tons, contributing to CO_2 emissions of nearly 1.45 Gt². This accounts for about 7% of the world's total emissions⁵. Addressing these environmental challenges involves enhancing the mechanical characteristics of cement, thereby extending the life cycle of structures. By utilizing high-performing cement, it becomes possible to significantly reduce the amount of cement required in concrete structures, thereby decreasing CO_2 emissions associated with its production^{2,6}.

Recent advancements in nanotechnology and nanomaterials offer promising opportunities to develop nano-enhanced materials that can improve the energy efficiency and environmental sustainability of structural materials like concrete⁴. Extensive research in this field has focused on manipulating the composition of cement at the nanoscale using various nanoreinforcing agents. Carbon nanostructure (CNS), including Carbon nanotube (CNT) and graphene, have garnered significant attention due to their remarkable physical and chemical properties⁷. Incorporating CNS

at very low concentrations holds great potential for substantially enhancing the performance of cement-based materials, improving mechanical strength, chemical resistance, and transport capabilities^{2,6}. These advancements hold substantial potential for extending the lifespan of construction projects and reducing the quantity of required concrete material.

Nevertheless, despite the significant potential of CNS in cement modification, poor dispersion quality prevents its widespread application². Successful applications necessitate the individual dispersed or formation of small bundles of CNS^{8,9}. However, the smooth surface and lack of active groups on CNS make them chemically inert and incompatible with many solvents¹⁰. Moreover, the presence of Van der Waals (VdW) attraction forces, attributed to their large surface area and high aspect ratio, tends to keep CNS in close proximity, leading to the formation of agglomerates or entanglements¹¹.

Numerous investigations have been conducted to disperse CNS using both physical (dispersion) and chemical (covalent and non-covalent functionalization) methods^{9,10}. However, these methods often involve tedious, multi-step processes typically achievable only at the laboratory scale. Additionally, these methods can inherently damage the structure and mechanical properties of carbon nanotubes to a certain extent, impacting their overall utility¹⁰.

In this work, we aim to produce a Nano-engineered cement by directly incorporating CNS into the cement matrix by two approaches: in-situ *via* Chemical vapor deposition (CVD) and ball milling. Firstly, a graphene-cement composite is developed by CVD using two carbon precursors: i) pure glucose, and ii) glucose mixed with iron chloride ($g/FeCl_3$) at a concentration of 0.5 wt% of the cement ratio, at temperatures of 800 and 1000 °C. In a second experiment, graphene is initially synthesized by CVD using $g/FeCl_3$ as the carbon precursor and further milled with cement to induce mechanical functionalization. The structural analysis, surface morphology, and surface interactions of the nano-engineered cement are characterized using Raman spectroscopy, XRD, XPS, and SEM to evaluate the efficiency in preparing a Nano-engineered cement composite. Additionally, mortar specimens are prepared to assess the mechanical strength of the nano-engineered cement.

Chapter 2

Theoretical Background

2.1 Nanotechnology

Dr. Richard Phillips Feynman, an American physicist and Nobel Laureate, is credited with pioneering nanotechnology. In his paper titled "There's Lots of Room at the Bottom," delivered on December 29, 1959, Feynman introduced the concept of directly manipulating individual atoms, proposing it as a more potent method for synthetic chemistry compared to the techniques available at that time¹².

Nanotechnology, an emerging field of study, focuses on the analysis of materials smaller than 100 nm, known as nano-materials¹³. Nanoscience, on the other hand, delves into understanding the properties and behaviors of these materials¹⁴.

Materials at the nanoscale exhibit unique characteristics compared to their larger-scale counterparts. For example, if a 1 cm gold cube is fragmented into nanoscale pieces, the resulting fragments will possess a significantly larger surface area than an equivalent amount of material at a larger scale. At this level, the nanoscale effect, often termed the "size effect," becomes apparent. The material's chemical reactivity is enhanced, influencing its electrical, magnetic, morphological, structural, thermal, optical, and mechanical properties. The melting point of bulk gold, previously at 1063 °C, may decrease to 500 °C. Furthermore, the once consistent color of the material now varies based on the size of each piece, with pieces of different sizes displaying colors ranging from blue to red on the spectrum¹³. At this scale, classical (Newtonian) mechanics are no longer sufficient to describe these properties, and quantum mechanics is employed to explain various observed phenomena.^{12,13}

In recent years, advancements in nanostructure science and technology have been notable, carrying significant commercial implications and promising even greater impacts in the future¹⁴.

The field of nanotechnology, which involves the fabrication of nanomaterials, can be categorized into two main approaches: top-down and bottom-up:

Top-Down

Top-Down, from top (great) to down (small), mechanisms focuses on the miniaturization of structures to the nanoscale. This approach has been the most widely utilized aspect of nanotechnology, with particular prominence in the field of electronics.¹².

Bottom-Up

Bottom-Up, from bottom (small) to top (large), start with nanometric structures, such as atoms or molecules. Through self-assembly or assembly processes, mechanisms or devices larger than the initial ones are created. Various production methods, including sol-gel, CVD, and laser pyrolysis, are employed in this category. For instance, some of these methods are employed in the manufacturing of CNT¹³.

Thus, by considering the impact of size on material properties, it becomes evident that an entirely new world exists at the nanoscale. Widely known materials exhibit completely different behaviors when they are totally at the nanoscale. These novel properties observed at the nanoscale offer a wide range of new applications, new materials, and new technologies explored by the fields of nanoscience and nanotechnology¹².

2.2 Carbon allotropes

Carbon stands as one of the fundamental building blocks of life on Earth owing to its ability to form stable chemical bonds with other carbon atoms and many other elements. Carbon, the sixth element in Mendeleev's Periodic Table, has four valence electrons, which leads to a variety of bonds with different hybridization of the valence orbitals¹⁵. Carbon exhibits three distinct hybridization states: sp , sp^2 , and sp^3 , each associated with a unique archetype, giving rise to a diverse forms of carbon allotropes^{15,16}, as shown in Fig. 2.1. Specifically, sp hybridization results in a linear (1D) carbyne structure, sp^2 hybridization leads to planar (2D) graphene and graphite, and sp^3 hybridization produces spatial (3D) diamond and alkanes¹⁵.

Graphite (pencil) and diamond have long been the familiar forms of carbon found in nature. Over the past few decades, new synthetic carbon allotropes like CNT, fullerenes, and graphene have been discovered¹⁶. Among these, CNT and graphene stand out for their exceptional physical and chemical properties, making them prominent materials in the field of nanotechnology¹⁷.

2.3 Graphene

Graphene is a 2D single-atom-thick sheet tightly packed with carbon atoms, spaced 1.42 Å apart with a bonding angle of 120°, forming a pattern resembling a honeycomb¹⁸, as illustrated in Fig. 2.2a. The valence electrons of the carbon atoms in the lattice occupy three in-plane sp^2 hybrid orbitals, which are responsible for the covalent bonding, with the p_z orbital extending out of the basal plane (Fig. 2.2b), responsible for the electronic properties^{19,20}. This structural arrangement gives graphene excellent thermal conductivity (3000 W $m^{-1}K^{-1}$), mechanical stiffness (1060 GPa), optical transparency (490%), charge carrier mobility (2000–20,000 $cm^2 V^{-1}s^{-1}$), and specific surface area

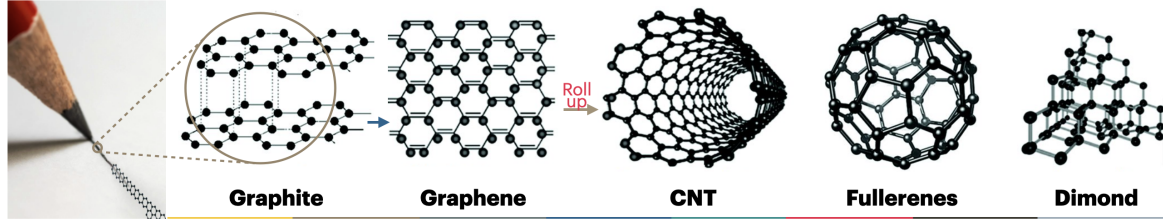


Figure 2.1: Various forms of carbon nanomaterials. (The image above is adapted from, Ref¹⁶)

($2,630 \text{ cm}^2 \text{ g}^{-1}$), plus fascinating phenomena such as the quantum Hall effect, spin resolved quantum interference, ballistic electron transport, and bipolar super-current, to name a few^{21,22}. These electronic properties were confirmed following the successful separation of monolayer graphene using scotch tape by Novoselov and Geim²³. Consequently, graphene has become one of the most extensively studied materials in physics and chemistry, with ongoing exploration for new applications²¹.

2.3.1 Graphene electronic structures

The two dimensional structure of graphene gives rise to a unique band structure that can be derived theoretically. To determine the lattice vectors, graphene is broken into two sub-lattices, A and B (as illustrated in Fig. 2.2c), where a_1 and a_2 can be expressed as²¹.

$$\mathbf{a}_1 = \frac{a}{2}(3, \sqrt{3}), \quad \mathbf{a}_2 = \frac{a}{2}(3, -\sqrt{3}) \quad (2.1)$$

where $a = 1.42 \text{ \AA}$ is the length of covalent bonds between carbon atoms in the A and B sites.

The reciprocal lattice vectors b_1 and b_2 (Fig. 2.2d) can then be computed as:

$$\mathbf{b}_1 = \frac{2\pi}{3a_0}(1, \sqrt{3}), \quad \mathbf{b}_2 = \frac{2\pi}{3a_0}(1, -\sqrt{3}) \quad (2.2)$$

The reciprocal lattice geometry of graphene is described by its symmetrical points within the Brillouin zone, known as the Dirac points, labeled as \mathbf{K} and \mathbf{K}' . These points possess specific K-space vectors:

$$\mathbf{K} = \frac{2\pi}{3a}(1, \sqrt{3}/3), \quad \mathbf{K}' = \frac{2\pi}{3a}(1, -\sqrt{3}/3) \quad (2.3)$$

The atomic structure results in a zero bandgap, where the conduction and valence bands converge at the cone-shaped vertices, as shown in Fig. 2.2e. Each vertex meets at the K-point of the Brillouin zone to form the Fermi level²⁴. The linear shape of the dispersion curve near the Dirac point is fundamentally distinct from the parabolic shape observed in typical semiconductors²¹. These unique properties of single-layer graphene make it suitable for various applications, including flexible displays, solar cells, and transparent electrodes, thanks to its outstanding crystallinity, high chemical stability, and impermeability²⁴.

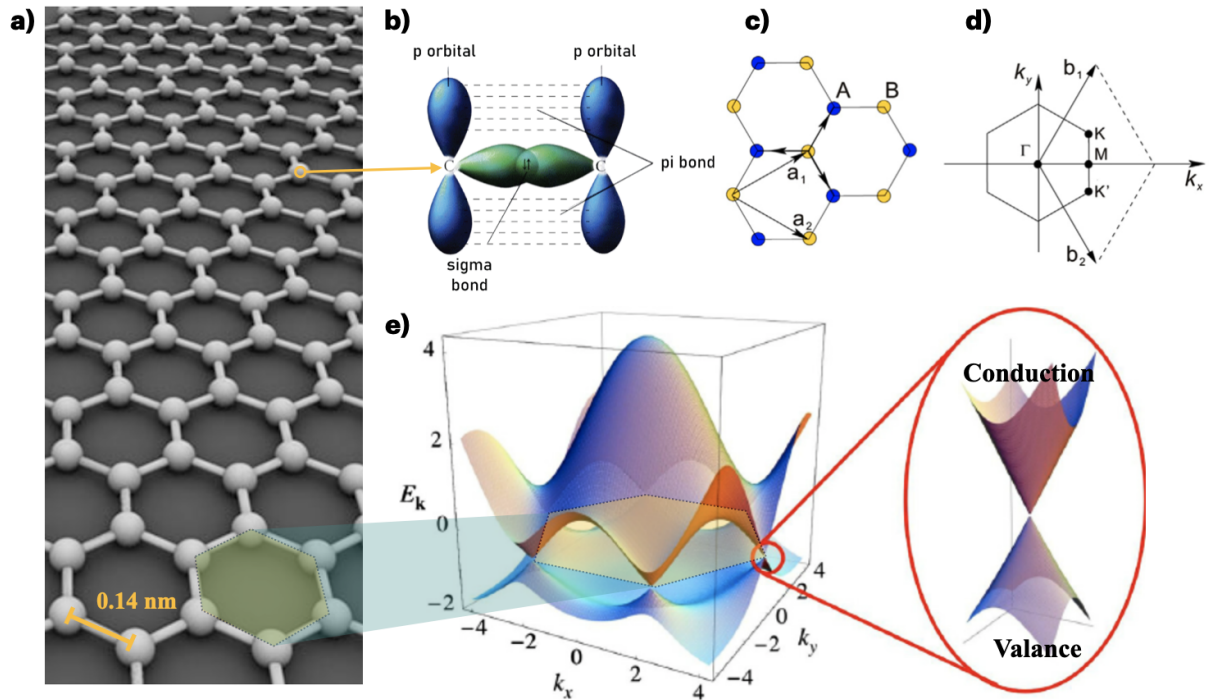


Figure 2.2: a) Graphene structure (adapted from Ref.²⁵). b) sp^2 orbitals oriented in the x and y planes with a trigonal planar shape, with the remaining p_z orbital perpendicular to the plane. c) 2D hexagonal lattice of graphene in real space, with vectors \mathbf{a}_1 and \mathbf{a}_2 . d) The first Brillouin zone with high symmetry points Γ , K, and M, and the reciprocal lattice with lattice vectors \mathbf{b}_1 and \mathbf{b}_2 . e) Representative electronic band structure of graphene, with the conduction and valence bands converging at cone-shaped vertices. These vertices meet at the K-point of the Brillouin zone, forming the Fermi level. Figures c, d, and e are adapted from Ref.²⁶.

2.3.2 Graphene mechanical properties

The mechanical properties of graphene is due to the stability of the sp^2 bonds that constitute the hexagonal lattice and resist various in-plane deformations²⁷. Despite consisting of only one atomic layer, graphene's sp^2 carbon atoms are held together by covalent σ -bonds, known for their exceptional strength, providing graphene remarkable stretchability and flexibility²⁴.

The mechanical properties of free-standing monolayer graphene were first measured by Lee et al.²⁸, who acclaimed graphene as "the strongest material ever measured". In their study, they fabricated suspended graphene structures by punching holes in a SiO_2 wafer and analyzed them using atomic force microscope (AFM). The theoretical breaking strength of graphene is approximately 40 N/m , with an elastic stiffness of around 1.0 TPa ²⁴.

Graphene's superior mechanical properties make it an ideal candidate for integration into various composite

materials to strengthen and enhance their performance. When integrated into materials like cement with a hydraulic matrix, graphene not only increases their mechanical strength but also enhances their durability and resistance to environmental factors such as moisture and chemical corrosion. This potential improvement in composite materials can revolutionize the construction industry by producing more durable and sustainable building materials⁶.

2.3.3 Graphene synthesis

Since the pioneering extraction of graphene in 2004²³, diverse methods have been established for graphene synthesis through two approaches: top-down and bottom-up. The most common top-down methods include mechanical and chemical exfoliation, while CVD stands out as a key approach for bottom-up synthesis. Chemical exfoliation and CVD methods show the greatest promise for bulk production of graphene at the scale necessary for composites applications^{17,22}. Among the two methods, the CVD is considered to be optimal to synthesize large-scale monolayer graphene with respectable quality, rendering it particularly suitable for display applications²⁴. The two methods are described in brief below.

Mechanical exfoliation

The mechanical exfoliation of graphene stands as the simplest method, initially introduced by Nobel laureates Geim and Novoselov²³. In this method, a piece of graphite undergoes repeated tape exfoliation (Fig. 2.3a). Since graphite is composed of stacked graphene layers held together by VdW interactions, exfoliation can rupture the weak interaction and extract a single layer of graphite, i.e., graphene¹⁷. Although mechanical exfoliation can yield high-quality monolayer graphene, its scalability is limited, making it mostly suitable for lab-scale experiments and prototyping due to challenges in scaling up^{24,27}.

Chemical vapor deposition

CVD stands out as one of the most effective methods to synthesize large-scale monolayer graphene with high structural quality.^{17,24} The method consist of exposing a metal to different hydrocarbon precursors at high temperatures, as illustrated in Fig. 2.3b)²⁷. These metal substrates should possess lattice structure that matches with the honey comb lattice of graphene, such as Ni(111) and Cu(111)^{21,27}. Graphene grows on the surface of a metal substrate through the decomposition of a carbon precursor, such as CH₄, which reacts with the surface at specific temperatures or pressures. Both Cu and Ni can yield high-quality single and few-layer graphene of identical quality, but the specific growth methods differ, as shown in Fig. 2.3c and d.

On the copper substrate, the carbon precursor decomposes on the surface, generating carbon atoms that migrate to active sites initiating the nucleation of graphene crystals aligned with the lattice spacing of the substrate. Similarly, on the Ni substrate, the carbon precursor undergoes decomposition. However, in this case, the free carbon atoms dissolve in the heated nickel substrate. As the substrate cools, the carbon ascends to the surface, forming a graphene sheet that matches the lattice spacing of the substrate. Empirical evidence has demonstrated that graphene grown through CVD exhibits exceptionally high quality, with properties closely approaching those predicted by theoretical models²¹.

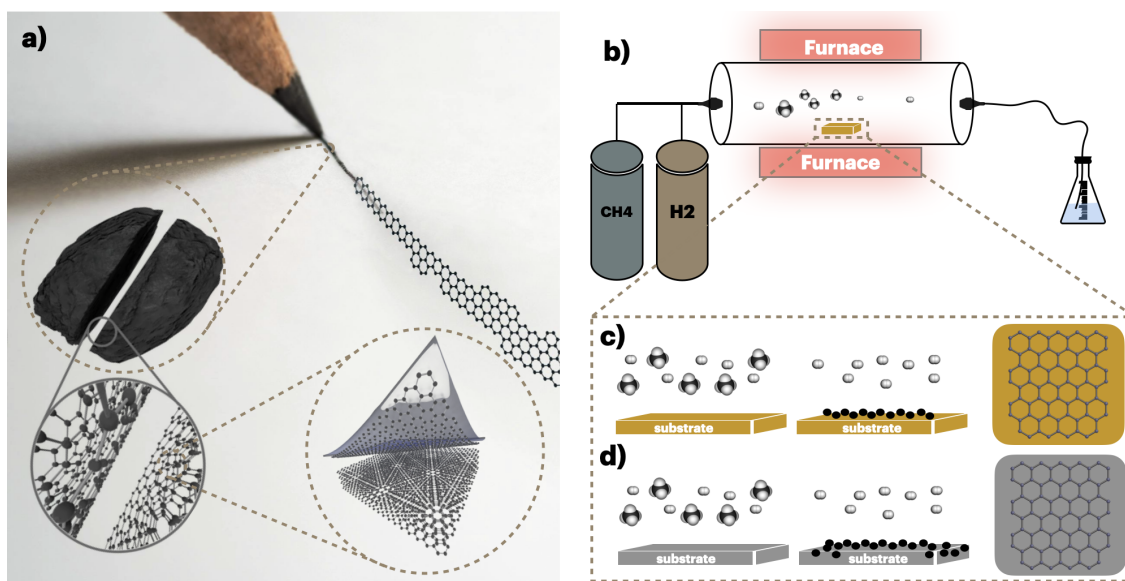


Figure 2.3: Most common synthesis methods of graphene. a) mechanical exfoliation using scotch tape. b) Representative schema of a CVD system, c and d) shows the schematic illustration of graphene synthesis mechanism on Cu and Ni foil, respectively.

2.4 Carbon nanotubes

CNT, introduced by Iijima in 1991²⁹, consist of hexagonally rolled layers of graphene with diameters ranging from a few nanometers to a few micrometers in length, featuring a half-fullerene structure at each end³⁰. Depending on the number of rolled graphene sheets, CNTs can be classified into Single-walled carbon nanotubes (SWCNT) or Multi-walled carbon nanotubes (MWCNT), as depicted in Fig. 2.4a and b. In MWCNTs, layers are held apart by the attractive VdW force³¹. The covalent bonding between sp^2 -hybridized carbon atoms provides CNTs with exceptionally high modulus ($\approx TPa$) and tensile strength (100–150 GPa), as well as other remarkable mechanical properties. Moreover, the CNT network exhibits significant electrical and thermal conductivities, thereby promoting their versatile applications as structural health monitoring sensors and as reinforcement in lightweight structural composites, leading to enhanced electrical conductivity and electromagnetic shielding^{31,32}. The multifunctionality of CNTs, coupled with their exceptional elastic modulus, low weight, and high aspect ratio, are the primary motivating factors for incorporating it as the reinforcement or filler for modern composite materials³². In fact, NASA is developing materials taking advantage of the high mechanical strength and modulus of CNTs for applications in space missions. It is believed that CNTs' reinforced composites may lead to production of materials with the greatest specific resistance (σ_{max}/ρ) ever manufactured by humans³⁰.

2.4.1 CNT electronic Structure

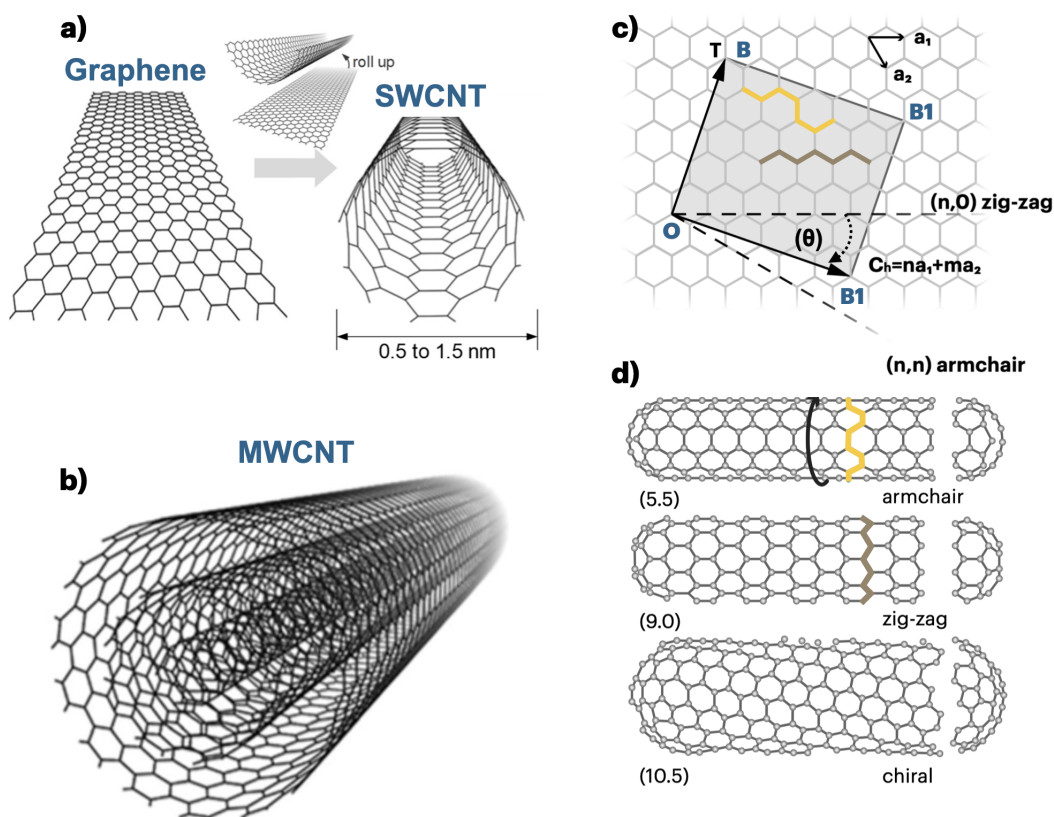


Figure 2.4: a) Conceptual diagram of single-walled carbon nanotube (SWCNT). b) Multi-walled carbon nanotube (MWCNT). c) Schematic of a two-dimensional graphene sheet illustrating lattice and the chiral vectors. d) The vectors representing cases of armchair, zigzag and chiral. (Adapted from, Ref³³)

In the preceding topic, we observed that the Fermi surface of an ideal graphene sheet consists of six corner K-points. However, when a graphene sheet is rolled up to create tubes, only a specific set of κ -states from the planar graphene sheet is permitted due to the periodic boundary conditions imposed in the circumferential direction. The permissible k-vectors of tubes are contingent on the diameter and chirality of the tubes. Predictions indicate that CNTs can exhibit metallic or semiconducting properties depending on their diameter and the chirality of the arrangement of graphitic rings in the walls³⁴.

The general principles to describe the atomic structure in terms of helicity or chirality defined by the chiral vector, C_h , and chiral angle, θ , are as follows.

The chiral vector should be described in terms of chiral indexes (n, m) and the unit vectors \mathbf{a}_1 and \mathbf{a}_2 (see Fig.

2.4a) by the equation³⁰;

$$\mathbf{C}_h = n\mathbf{a}_1 + m\mathbf{a}_2 \quad (2.4)$$

where (n, m) are integers representing the number of steps along the carbon bonds of the zigzag hexagonal lattice. The module of the unit vectors \mathbf{a}_1 and \mathbf{a}_2 has value of

$$|\mathbf{a}_1| = |\mathbf{a}_2| = a = 0.246 \text{ nm} \quad (2.5)$$

The C – C bond length (a_{C-C}) can be related to a unit vector by

$$a_{C-C} = \frac{a}{\sqrt{3}} = 0.142 \text{ nm} \quad (2.6)$$

The θ determines the degree of “twisting” of the tube and is defined as the angle between the vectors \mathbf{C}_h and \mathbf{a}_1 , which varies in the range $0^\circ \leq |\theta| \leq 30^\circ$. In terms of integers (n, m) , θ can be described by the following set of equations;

$$\sin\theta = \frac{\sqrt{3}m}{2\sqrt{n^2 + m^2 + nm}} \quad (2.7)$$

$$\cos\theta = \frac{2n + m}{2\sqrt{n^2 + m^2 + nm}} \quad (2.8)$$

$$\tan\theta = \frac{\sqrt{3}m}{2n + m} \quad (2.9)$$

Depending upon the rolling direction in the plane of a graphene sheet, CNTs are classified into three unique geometries, as illustrated in Fig. 2.4d:

- For zigzag CNT ($\theta = 0^\circ$), $n = \text{integer}$, $m = 0$; for example, $(n, m) = (9, 0)$.
- For armchair CNTs ($\theta = 30^\circ$), $n = m = \text{integer}$; for example, $(n, m) = (5, 5)$.
- For chiral CNTs ($0^\circ < |\theta| < 30^\circ$), $n, m = \text{integer}$, $n \neq m$; for example, $(n, m) = (10, 5)$.

A nanotube is metallic (conductive) either when $n = m$ or when $n - m$ or $m - n$ are multiples of 3, or m and n take values that satisfy the relation $|m - n| = 3i$ (where i is an integer) as $(3, 0)$, $(7, 1)$, $(8, 5)$, etc. Therefore, all armchair nanotubes are metallic because $n - m = 0$. For all other cases, $|m - n| \neq 3i$, nanotubes are semiconductors with a band gap energy of around 0.5 eV ³⁰.

Also, as the inter atomic spacing between the carbon atoms is known, the diameter of a nanotube (d) can be calculated as the ratio between the circumference of the tube L and π

$$d = \frac{L}{\pi} = \frac{\sqrt{n^2 + nm + m^2}a}{\pi} \quad (2.10)$$

or in terms of n , m , and b

$$d = \frac{C_h}{\pi} = \frac{\sqrt{3(n^2 + nm + m^2)}b}{\pi} \quad (2.11)$$

for large diameter CNT ($\frac{1}{\text{radius}} \ll 1$), the electrical nature depends upon the chiral vector³².

2.4.2 CNT mechanical properties

CNTs, formed by rolling graphene with exceptionally strong chemical bonds, are expected to possess high mechanical properties. In theory, pristine CNTs have well-defined atomic positions and a stable chemical structure, determined by the rolling direction of the graphene sheet. However, in practice, imperfections such as chemical impurities, atomic vacancies, and Stone–Wales defects are commonly present in the hexagonal structure of CNTs, significantly impacting their elastic and inelastic response³².

Table 2.1 compares the mechanical properties of nanotubes to other materials. Notably, the density of CNTs is approximately five times lower, while the Young’s modulus is roughly five times greater than that of steel. This combination of extremely high strength coupled with low density makes nanotubes one of the most attractive materials for applications requiring low weight and high strength, such as airplanes, space shuttles, wind turbines, boats, etc³⁰.

Material	$\rho(g/cm^3)$	E(GPa)	$\sigma_m(GPa)$	$\epsilon(\%)$
SWCNTs	1.33	1054	150	12
MWCNTs	2.6	1200	150	12
Carbon fiber M60JB	1.93	588	3.82	0.7
Glass fiber type "S"	2.48	86	4.58	5.4
Kevlar 49	1.44	112	3.00	2.4
Aluminum 2219-T87	2.83	73	0.46	10
Steel 17 - 7 PH RH950	7.65	204	1.38	6
EpoXy	1.25	3.5	0.005	4

ρ : Density; E: Young’s Modulus; ϵ : Elongation at Break; σ_m : Maximum Resistance.

Table 2.1: Mechanical Properties of Materials. Adapted form, Ref.³⁰.

2.4.3 CNT synthesis

Numerous synthesis methods have been developed for the production of CNTs. Among these methods, the three most successfully employed are arc discharge, laser ablation, and CVD processes. Notably, CVD stands out as the most cost-effective, scalable, and widely used method³⁶.

The growth process of CNT *via* CVD method involves decomposition of carbon source at high temperatures in the presence of catalysts. Commonly, iron, nickel, or cobalt is chosen as catalysts³⁵. The frequently utilized carbon

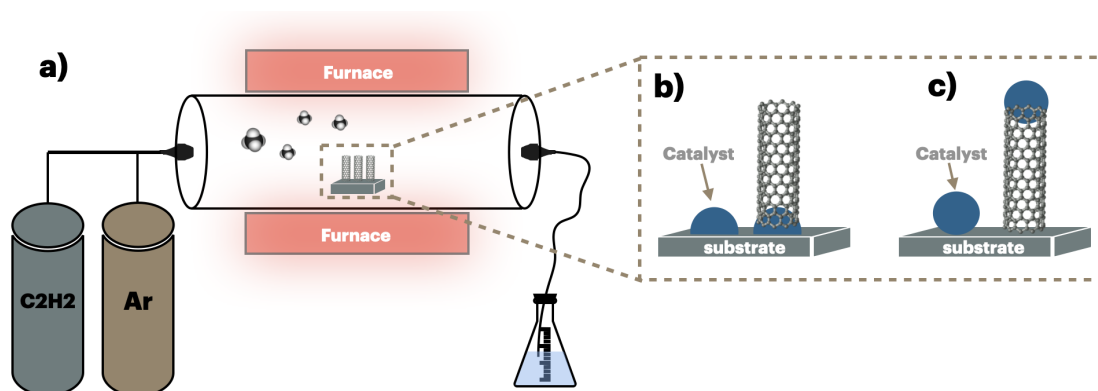


Figure 2.5: Representative schema of CNT synthesis *via* CVD. a) Classical CVD setup showing the carbon source, inert gas, and furnace. b) Illustration of a strong interaction mechanism involving catalyst nanoparticles firmly attached to the substrate, serving as sites for CNT growth. c) Representation of a less stable interaction mechanism where the catalyst separates from the substrate during carbon atom deposition.³⁵

sources include ethylene, acetylene, methane, carbon monoxide, and ethanol³⁶. The CVD process can be described as follows: firstly, the hydrocarbon source decomposes to form carbon atoms due to the presence of heat or plasma. These carbon atoms are then adsorbed on the surface of the catalyst.³⁷

Fig. 2.5a, illustrates a schematic of a classic reactor used for synthesizing CNTs *via* CVD. It consists of a hydrocarbon source gas, carrier gas, a furnace, and an outlet tube. A substrate with a previously deposited precursor is heated to the appropriate temperature (typically between 500°C and 1200°C), and a mixture of carrier gas and a carbon source is introduced. Metallic particles act as structure director agents, inducing the formation of graphite walls and the tubular-like arrangement. There are two well-known routes on CNTs growth CNT³⁵.

In the first route, Fig. 2.5b, carbon atoms diffuse from the metallic particle surface attached to the substrate. In this process, the carbon atoms organize into rings that substitute the atoms previously formed, displacing the ring from the particle surface³⁵. Consequently, the top of the nanotube consists of the earliest attached carbon atoms, while the last atoms incorporated into the nanotube are on metallic catalyst nanoparticles attached to the substrate.

In the second route, when there is a weak interaction between the substrate and catalyst, the tip-growth model is preferential, involving the formation of initial graphene rings on nanoparticle catalysts attached to the substrate (Fig. 2.5c). Subsequently, the nanoparticle catalyst is detached from the surface as new carbon atoms are incorporated into the nanotube. Consequently, the last incorporated atoms are at the top of the nanotube, distant from the substrate where the nanotube formation initiated.

The CVD process offers the capability to synthesize both SWCNTs and MWCNTs. The control over the type of CNT produced is achieved through the selection of catalyst types, substrate types, hydrocarbon types, reaction time, and reaction temperature^{35,37}

2.5 Portland cement

Portland cement is a complex product made by heating a mixture of limestone and clay to a temperature of approximately $1450\text{ }^{\circ}\text{C}$ ³⁸. Very precise proportions of these two basic materials have to be mixed with some additions to produce a raw meal with a precise chemical composition³⁹. Beyond $1450\text{ }^{\circ}\text{C}$, partial fusion occurs, involving the transformation of the oxides of calcium, silicon, aluminum and iron in the clinker, as illustrated in Fig 2.6. The clinker is then mixed with a few per cent of calcium sulfate, which prevents immediate hardening upon contact with water, and is finely ground to produce the cement. The minerals formed are responsible for cement's hydraulic properties³⁸. In this work, the term 'clinker' is used instead of the expression 'Portland cement clinker'.

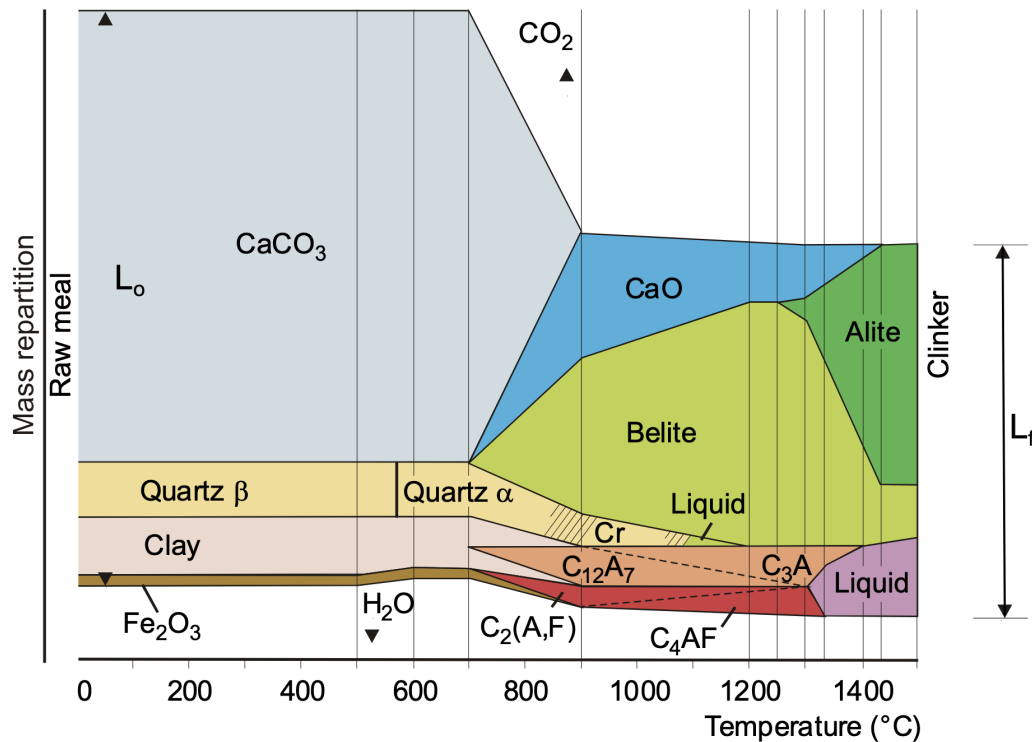


Figure 2.6: Phase diagram illustrating the transformation of raw meal into clinker. Adapted from, Ref.⁴⁰.

2.5.1 Mineral composition of Portland cement

The chemical composition of the raw feed is modified to facilitate the formation of four minerals, depicted in Table 2.2, which subsequently react with water to create bonds.

The clinker typically comprises approximately 67% CaO , 22% SiO_2 , 5% Al_2O_3 , 3% Fe_2O_3 , and 3% other

Minerals	Formula	Minerals	Symbols	Pseudo-chemical	Phase
Tricalcium silicate	$SiO_2.3CaO$	SiO_2	S	C_3S	Alite
Dicalcium silicate	$SiO_2.2CaO$	CaO	C	C_2S	Belite
Tricalcium aluminate	$Al_2O_3.3CaO$	Al_2O_3	A	C_3A	Aluminate
Tetracalcium ferroaluminate	$4CaO.Al_2O_3.Fe_2O_3$	Fe_2O_3	F	C_4AF	Ferrite

Table 2.2: To simplify the writing of the four minerals, the symbols proposed by ceramic science is used.

components. It normally consists of four major phases known as alite, belite, aluminate, and ferrite (see Table 2.2). Alite and belite constitute the silicate phase, while aluminate and ferrite make up the aluminous phase³⁹. Additionally, several other phases, such as alkali sulfates and calcium oxide, are typically present in minor amounts³⁸.

The hardening process results from reactions between these major phases and water. Here we provide a brief description and purpose of each major phase³⁸:

- **Alite** is the most important constituent of all clinkers, comprising 50-70% of its composition. C_3S is modified in its composition and crystalline structure by ionic substitutions. It reacts relatively quickly with water, and is the most important of the constituent phases for strength development, especially within the first 28 days.
- **Belite** constitutes 15-30% of clinkers and is typically found primarily as the β -polymorph, with some ionic substitutions. Belite reacts more slowly with water, contributing less to early strength but significantly enhancing it in later stages. After one year, pure alite and pure belite exhibit similar strengths under comparable conditions.
- **Aluminate** constitutes 5-10% of clinkers, which can undergo significant alterations in both composition and occasionally structure due to ionic substitutions. When exposed to water, aluminate reacts rapidly and may cause excessively fast setting unless a setting-controlling agent, typically gypsum, is introduced.
- **Ferrite** makes up 5-15% of clinkers and is substantially modified in composition by variations in the Al/Fe ratio and ionic substitutions. Its rate of reaction with water appears to be somewhat variable, possibly due to differences in composition or other characteristics. Generally, ferrite exhibits high initial reactivity but lower or very low reactivity at later stages.

2.5.2 The hydration of Portland cement

In cement chemistry, hydration refers to the reaction of non-hydrated cement or one of its constituents with water, involving both chemical and physico-mechanical changes in the system, particularly associated with setting and hardening⁴¹. The term "setting" refers to the abrupt loss of plasticity in the initial paste, transforming it into a solid material with minimal measurable strength. In contrast, 'hardening' denotes the progression of hardness and strength that occurs subsequent to the setting of the paste. The mechanism that occurs in hydration process begins

with the most soluble compounds that pass into an ionic aqueous phase and then precipitate to form the crystalline hydrated compounds⁴².

As Portland cement is a system with multiple components, its hydration is a intricate process comprising a series of individual chemical reactions that occur simultaneously and consecutively. The initiation of this process occurs spontaneously when the binder comes into contact with water and is accompanied by the release of heat⁴¹.

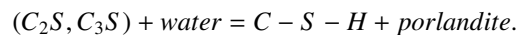
The water/cement ratio (w/c), representing the relative proportion of water to cement in the mixture, plays a crucial role in shaping the rheology of the resulting suspension, influencing the progress of hydration, and determining the characteristics of the hydrated material. In the range of water-cement ratios from approximately 0.3 to 0.6, the suspension exhibits a paste-like consistency, referred to as "fresh cement paste." This paste undergoes the processes of setting and hardening as hydration progresses, ultimately evolving into "hardened cement paste"⁴¹.

The advancement of hydration and its kinetics can be affected by various factors, particularly⁴¹:

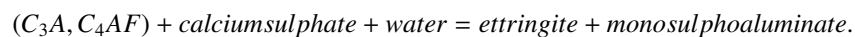
- by the phase composition of the cement and the presence of foreign ions within the crystalline lattices of the individual clinker phases;
- by the fineness of the cement, in particular by its particle size distribution and specific surface;
- by the water-cement ratio used;
- by the curing temperature;
- by the presence of chemical admixtures, i.e. chemical substances added in small amounts to modify the hydration rate and properties of the cement paste;
- by the presence of additives, i.e. materials interground with cement in larger amounts, such as granulated blast furnace slag or pulverised fly ash.

When C_3S and C_2S react with water, they undergo a transformation into calcium silicate hydrate and hydrated lime ($Ca(OH)_2$). The specific chemical composition and structure of the calcium silicate hydrate vary considerably, thus it is commonly denoted by the general formula Calcium silicate hydrates (C-S-H). In hydrated cement paste, the crystalline form of hydrated lime is referred to as **portlandite**. Notably, the hydration of C_3S generates a greater amount of portlandite compared to the hydration of C_2S due to the higher lime content in C_3S ³⁹.

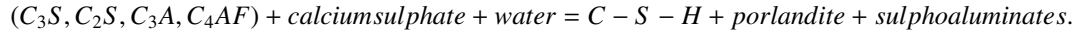
The hydration reaction of C_3S and C_2S can be represented schematically by the following equation:



In the presence of calcium sulphate, the interstitial phase (C_3A, C_4AF) is transformed into ettringite and monosulphoaluminate according to the following equation:



Combining these two equations, the following equation is obtained:



C-S-H is responsible for developing strength, while Portlandite is responsible for maintaining a high pH and therefore protecting the steel reinforcement in a structure. And the presence of sulfoaluminate can accelerate the hydration of silicates^{41,43}.

2.6 Nanocomposites

Conventional composites can be defined as combinations of two materials, with one acting as the reinforcing phase (in the form of fibers, sheets, or particles) embedded in the other material acting as the matrix phase. Reinforcing materials typically possess strength and low densities, while the matrix phase is usually composed of a ductile or tough material. The effective combination of these materials combines the strength of the reinforcement with the toughness of the matrix, resulting in a combination of desirable properties not found in any single conventional material. As an example, the ancient Egyptians crafted Adobe brick composites for civil engineering structures by using a mixture of mud and straw, creating a composite material that exhibited greater strength than either mud or straw on its own⁴⁴.

Following a similar principle, modern construction employs steel reinforcement in concrete. Steel, being ductile, is effective for tension but lacks compressive strength. Conversely, concrete, being brittle, performs well under compressive loading but lacks reliable tension resistance. Consequently, the incorporation of thin steel bars into concrete creates a new material with improved behavior in both tension and compression modes⁴⁴.

Similarly, Nanocomposites are defined as composite or multiphase materials where at least one phase has a dimension in the nanoscale range ($10^{-9}m$)⁴⁵. These materials are currently finding applications across a wide range of sectors, from nanoelectronics to the energy storage industry, owing to their exceptional electronic, mechanical, and chemical properties⁴⁶. These materials, considered the materials of the 21st century, possess unique design characteristics and property combinations not typically found in conventional composites⁴⁵.

Similar to microcomposites, nanocomposite materials can be categorized into three distinct groups based on their matrix materials, as delineated in Table 2.3: Ceramic Matrix Nanocomposites (CMNC), Metal Matrix Nanocomposites (MMNC), and Polymer Matrix Nanocomposites (PMNC)^{45,47}. Among the variety of nanocomposites, carbon-based nanocomposites have received considerable attention in the past two decades owing to their structure-dependent electronic properties, low density, and substantial specific surface area⁴⁶.

It is worth mentioning that due to the fact that the main focus in this work will be on the graphene and CNT-reinforced nanocomposites, the discussions will be orientated to be about such nanocomposites. However, the concepts are generalizable and readers can use them to understand what happens in other types of nanocomposites.

Material	Examples
Metal	<i>Fe – Cr/Al₂O₃, Ni/Al₂O₃, Co/Cr, Fe/MgO, Al/CNT, Mg/CNT</i>
Ceramic	<i>Al₂O₃/SiO₂, SiO₂/Ni, Al₂O₃/TiO₂, Al₂O₃/SiC, Al₂O₃/CNT</i>
Polymer	Thermoplastic/thermoset polymer/layered sili-cates, polyester/TiO ₂ , polymer/CNT, polymer/layered double hydroxides

Table 2.3: Different types of nanocomposites. Adapted form, Ref.⁴⁵.

2.6.1 Carbon based nanostructured cement

Materials based on cement, like concrete, are commonly described as quasi-brittle substances due to their inherent characteristics of low tensile strength and limited strain capacity, which makes it more susceptible to cracks. Typically, reinforcement of cementitious materials occurs at the millimeter or microscale using macrofibers and microfibers, respectively. However, while microfibers can delay the formation of microcracks, they do not prevent their initiation. This, in turn, permits the flow of chemical and water, leading to performance degradation⁴.

The incorporation of fibers at the nanoscale offers the opportunity to manage cracks at that level, potentially giving rise to a novel generation of 'crack-free materials'^{*4,50}. Materials modified at the nanoscale exhibit significantly enhanced mechanical, electrical, and thermal properties in comparison to those at the micro and macro scales. This enhancement results from the relatively larger surface area at the nano level, which increases chemical activity and influences strength and electrical characteristics¹.

Carbon nanostructures, in particular, are considered ideal for fabricating smart cementitious composites due to their piezoresistive features. This emerging cement, often termed "smart cement," can translate mechanical strain into changes in electrical properties, such as resistance and reactance¹. Consequently, the self-sensing capability of concrete is achieved by modifying the conductive network within the material⁵⁰.

The great interest in incorporating CNT and graphene into the cement-based composites are associated with the following features and contributions Lin and Du⁶, Singh⁵¹:

- CNTs accelerate hydration and decrease nanoporosity in cement paste.
- They act as nucleating agents for C-S-H gel and decrease shrinkage while increasing ductility.
- Addition of CNTs improves thermal conductivity and thermal-storage performance.
- Graphene/CNT infusion reduces cement consumption for identical mechanical properties.
- They enhance resistance to aggressive environments and enable strain/damage sensing in civil infrastructures.
- CNS in cement composites have diverse applications, including static/dynamic wireless charging on road pavement, prevention of thermal cracking, improvement of fire resistance, de-icing capability, and exceptional electromagnetic interference shielding for enhanced privacy and minimized health risks, as shown in Fig. 2.7.

*Acting as reinforcement agents in composites, CNS bolster mechanical properties and impede crack formation and propagation owing to their high tensile strength and stiffness.

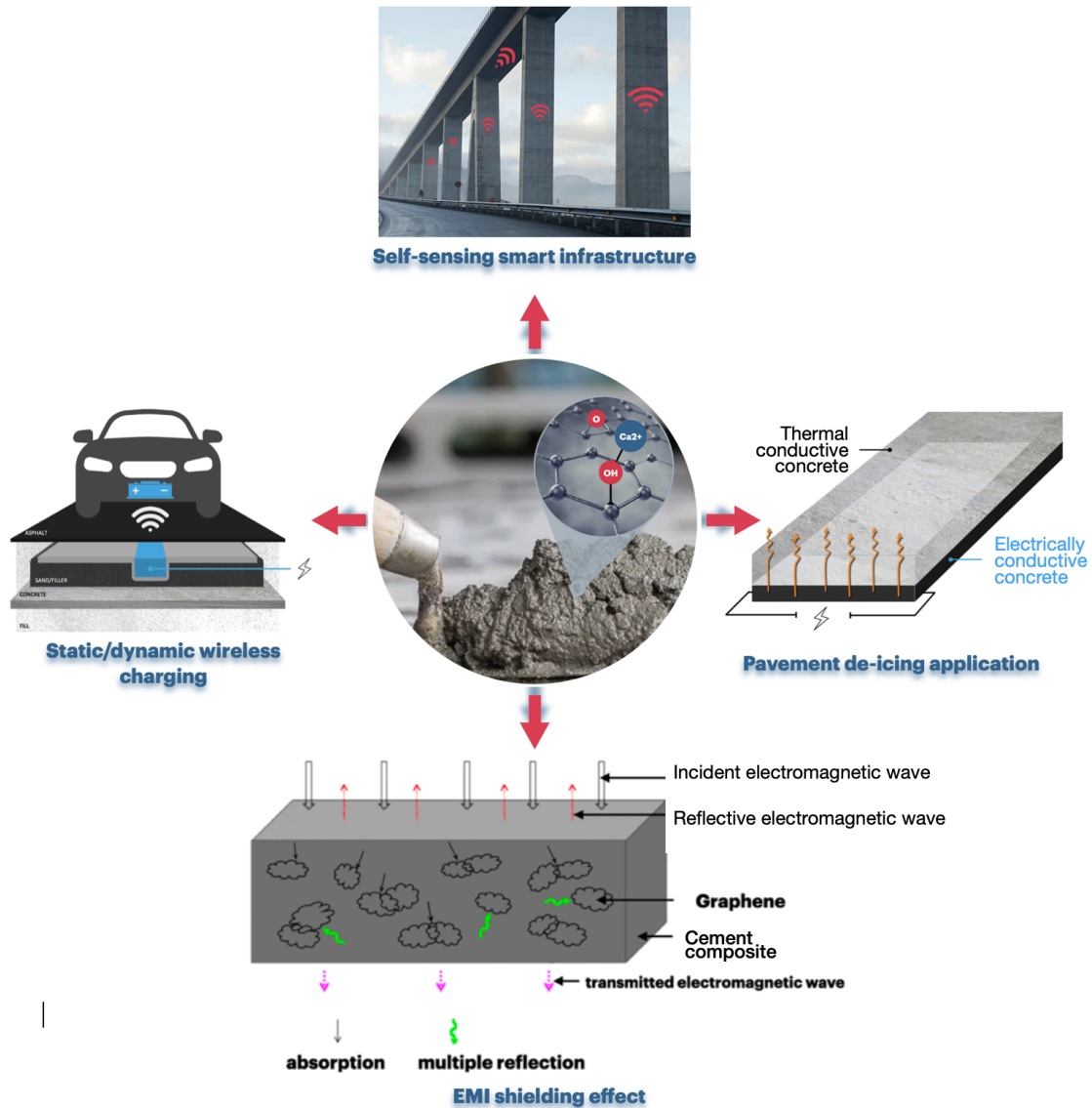


Figure 2.7: Schematic diagram of multifunctionality of graphene reinforced cement composites. Adapted from, Ref. ^{6,48,49}

Dispersion of Carbon nanostructure

Despite the promising applications of CNSs, their widespread utilization of carbon nanostructured cement remains limited due to processing difficulties². The primary challenge associated with the incorporation of carbon nanos-

structures in cement matrices is the poor dispersion. CNS, characterized by stable sp^2 hybridization and a lack of active groups, exhibit chemical inertness and incompatibility with numerous solvents¹.

As a result, the dispersion of carbon nanostructures in water is particularly challenging, attributed not only to VdW forces but also to the hydrophobic characteristics of the materials⁴. Inadequate dispersion in the cement matrix can lead to defects and constrain the nano-reinforcement effect in cement composites⁶.

Two primary approaches for dispersing CNS in water involve physical methods, which utilize dispersants for non-covalent surface modification employing ultrasounds, and chemical methods, which entail covalent surface modification^{1,6}.

Physical methods commonly employ ultrasonication to disperse carbon nanostructure into base fluids. Ultrasonic processors convert line voltage into mechanical vibrations, which are then transmitted into the liquid by the probe, generating microscopic bubbles. This phenomenon, known as cavitation², induces millions of shock waves. Despite the modest energy released by each individual bubble, the combined impact leads to the release of exceptionally high levels of energy, leading to the dispersion of CNS and surfaces within the cavitation field. In a typical procedure, carbon CNS are mixed in an aqueous solution containing various amounts of surfactant, and the resulting dispersions are sonicated at room temperature^{4,10}.

In contrast, the chemical approach employs surface modifications to enhance the surface functionality of carbon nanostructure. Essentially, the functionalization process involves the covalent attachment of functional groups onto the scaffold of carbon nanostructure. The treatment consist of strong acidic solution, like concentrated H_2SO_4 or HNO_3 , which can rupture the end-caps of the tubes and generate defects along the walls of the carbon nanostructure. Within these defects, oxygenated groups ($-COOH$, $-OH$) are linked to the scaffold, forming $CO = OH$, $C - O$, and $C - OH$ ⁵². The functional groups increases the reactivity and solubility and are used as platforms for integrating a variety of other complex groups.

2.7 Characterization techniques

2.7.1 Raman spectroscopy

Raman spectroscopy, as illustrated in Figure 2.8a, is a light-scattering technique that relies on the interaction of light with matter. This technique finds widespread application in chemistry and material science for providing a structural fingerprint that enables the identification of molecules⁵⁴. In 1930, handrasekhara Venkata Raman received the Nobel prize for his discovery that when light passes through a transparent medium, some of the scattering radiation undergoes changes in its wavelength⁵⁵.

The working principle of this technique is based on the interaction of a monochromatic beam of light with a atom or molecule. This interaction, occurring in a remarkably brief time frame of about 10^{-14} seconds or less, scatters a fraction of the radiation energy. During this brief period of time, the molecule is temporarily raised to a higher energy level called a “**virtual state**” or “**excited state**” and subsequently returns to a lower energy state after the light scatters⁵⁴.

The scattered light can be divided into two components, as show in Fig. 2.8b): firstly, the Rayleigh scattering,

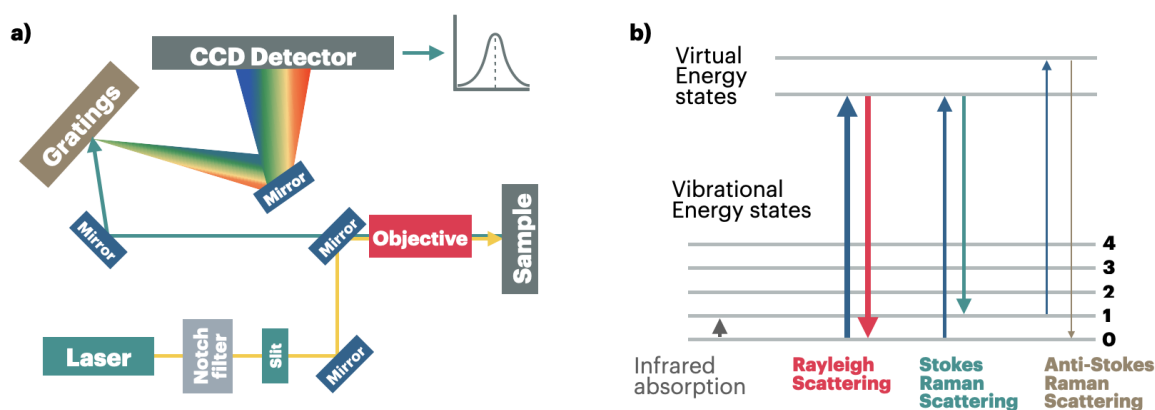


Figure 2.8: a) Optical path schematic of a Raman system (Adapted form, Ref.⁵³). b) Working principal of Raman technique⁵⁴.

sharing the same frequency (ν_o) as the incident light, and secondly, the Raman scattering, with a frequency of $\nu_o \pm \nu_R$, where ν_R represents the molecular vibration frequency. The lines $\nu_o + \nu_R$ and $\nu_o - \nu_R$ are named as anti-Stokes and Stokes lines, respectively. Thus, in Raman spectroscopy, one measures the molecular vibration frequency (ν_R) as a shift from the incident frequency (ν_o)⁵⁶. This alteration in the wavelength of the scattered photons, caused by changes in the **polarizability** of the molecules, provides the structural information or fingerprint of the sample⁵⁵.

2.7.2 Raman spectroscopy of Carbon allotropes

Raman spectroscopy is a fast, nondestructive, and high-resolution tool for the characterization of the lattice structure and the electronic, optical, and phonon properties of carbon allotropes⁵⁹. Through the combination of Raman band position, FWHM and intensity/area in the spectra, their structures can be analysed in terms of orientation, number of layers/walls, chirality, stacking order, defects and functionalisation⁶⁰. Thus, by doing the Raman characterization of carbon materials, one can get the information about the size, conductivity, chemical doping, and phonon structure of the materials⁵⁶.

Raman spectroscopy of Graphene

The phonon dispersion of graphene exhibits a total of six modes, three acoustic and three optical branches. Since graphene has two carbon atoms per unit cell, it possesses a total of six normal modes at the Brillouin zone center T. Among these modes, two are doubly degenerate. Hence, in the case of graphene, the irreducible representation obtained is $T = A_{2u} + B_{2g} + E_{1u} + E_{2g}$, where the phonons A_{2u} and E_{1u} are infrared active, while B_{2g} and E_{2g} are Raman active. This representation indicates the presence of one degenerate in-plane optical mode, E_{2g} , and one out-of-plane optical mode, B_{2g} ^{58,59}.

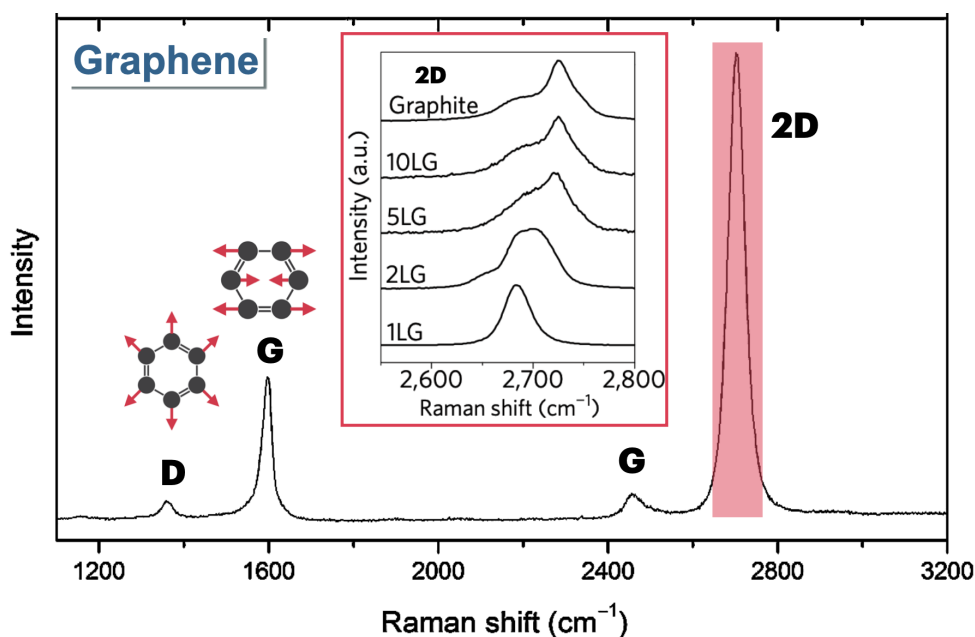


Figure 2.9: Raman spectroscopy analysis of graphene's vibrational modes, showcasing the distinct D and G lattice vibrations within the carbon ring, alongside the prominent 2D band (adapted from, Ref.⁵⁷). Inset figure adapted from, Ref.⁵⁸

The Raman spectrum of single layer graphene (Fig. 2.9) exhibits two prominent features. The G band, located at approximately 1580 cm^{-1} , corresponding to high frequency E_{2g} symmetry phonon at T Brillouin zone center. The intensity of this band is sensitive to the number of graphene layers, as well as the effects of strain and doping⁵⁷. Additionally, the G band is a common characteristic found in various graphitic materials, including carbon nanotubes. The D band, at approximately 1350 cm^{-1} , is associated with disorder or defects and is attributed to the breathing modes of six carbon ring atoms. Activation of this band requires the presence of defects, and its intensity is correlated with the density of defects. Additionally, there is a strong band at 2680 cm^{-1} , assigned to two-phonon scattering, known as the 2D band, which is an overtone of the D band. Since the 2D peak originate from a process where momentum conservation is satisfied by two phonons with opposite wave vectors, it does not require defects for activation and is consistently present⁵⁸. The position, form, and intensity of the 2D band are influenced by the number of graphene layers. In a graphene monolayer, the 2D band is singular, but as the number of graphene layers increases, it splits into several overlapping modes due to the reduction in symmetry, eventually resembling that of graphite, as illustrated in the inset figure of Fig. 2.9. Information about the number of graphene layers can be obtained from the intensity ratio of the G to 2D bands (I_G/I_{2D}) in the Raman spectrum⁵⁷.

Raman spectroscopy of CNT

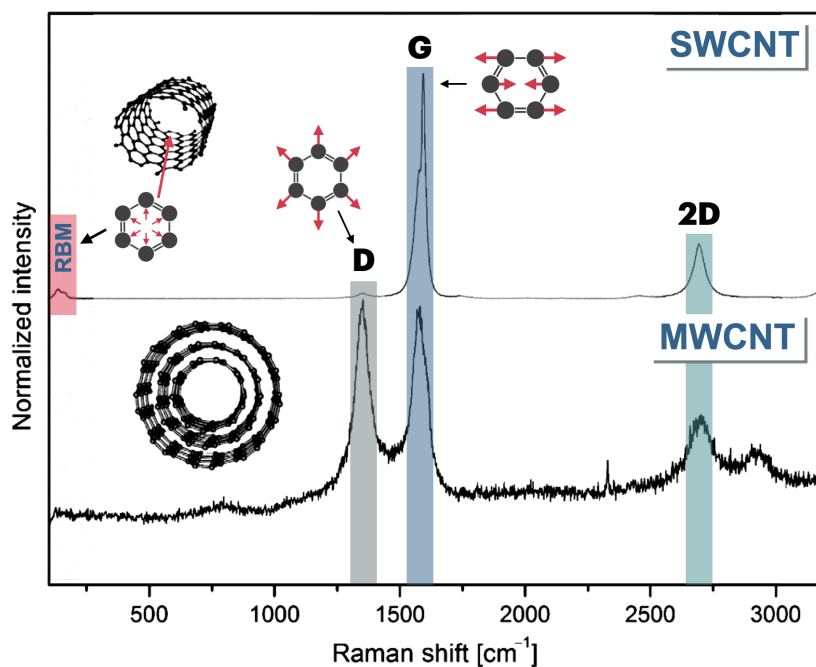


Figure 2.10: Raman spectra of SWCNT and MWCNT, depicting the G, D, and 2D bands. Additionally, SWCNT exhibits additional vibrations at lower Raman shifts known as radial breathing modes, which offers insights into the nanotubes diameters. Adapted from, Ref.⁵⁷

The Raman spectra of other graphitic materials, such as CNTs, can be analyzed based on the fundamental knowledge of graphene. However, other effects, such as curvature and stacking order, need to be taken into account⁶⁰. Fig. 2.10 depicts the Raman spectra of SWCNT and MWCNT, with its characteristic features: the G, D, and 2D band. The first noticeable difference between SWCNT and MWCNT is the band below 300 cm^{-1} , corresponding to the radial breathing mode (Radial breathing mode (RBM)) of SWCNT. This peak provides information about the electronic properties of the nanotubes and it is used for measuring the diameter of the CNTs, according to the equation:

$$\omega_{RBM} = \frac{A}{d_t} + B \quad (2.12)$$

where, A and B are experimentally determined parameters influenced by the environment and CNT type (e.g., the B constant describes the interaction in bundles of nanotubes or in the substrate)⁵⁷. RBMs are typically absent in MWCNT spectra due to the weak signal from the outer tube with a larger diameter and signal broadening caused by inner tube diameters⁵⁷. Another distinction lies in the shape of the G and D bands. SWCNT spectra typically

exhibits two distinctly separated G bands ($G +$ and G^*) and a more prominent D band. In the spectrum of MWCNTs around 3000 cm^{-1} , overtones ($D + G$), $2G$, and $2D$ are observed in the second-order Raman spectra⁵⁷.

2.7.3 X-Ray Diffraction (XRD)

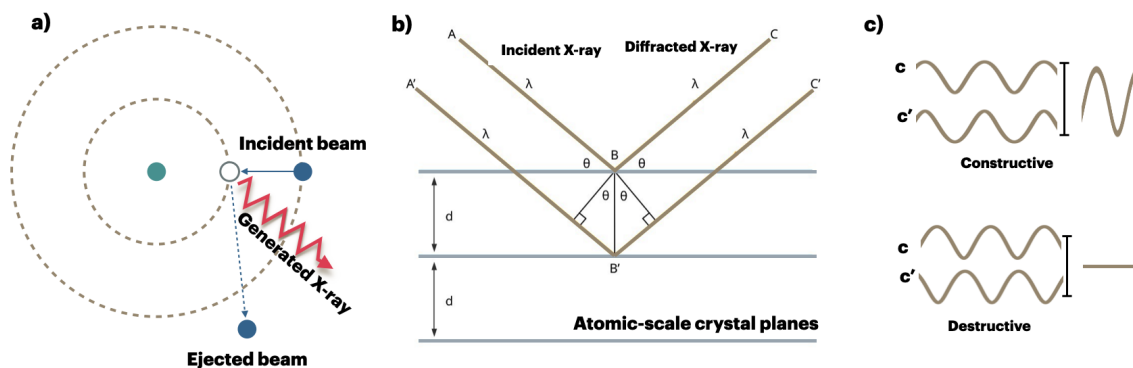


Figure 2.11: a) Schema of generation of X-ray, b) interaction of X-ray with the planes, and c) constructive and destructive interference

X-ray diffraction (XRD) is used to study the crystalline structure of materials since the X-ray wavelengths (between 0.2 and 10 nm) are comparable to the interatomic spacing of crystalline solids. The technique measures the average spacing between layers or rows of atoms. XRD allows us to determine the orientation of a single crystal or grain and to measure the size and shape of small crystalline regions. In XRD, a collimated beam of X-rays is scattered by the periodic lattice of the sample, as a result of the interactions of the photons with the electrons of the material using an elastic and coherent scattering process (Fig. 2.11a)). Each crystalline material has a discrete atomic structure, which upon irradiation with X-rays causes a constructive and destructive interference (Fig. 2.11c)) of the scattered X-ray beam, generating a unique diffraction pattern that presents several sharp spots, known as Bragg diffraction peaks.

The XRD of the crystalline sample reveals the presence of well-defined peaks at specific scattering angles, while the amorphous sample shows an intensity maximum that extends over several degrees (2θ). The diffraction of X-rays by a crystal (Fig. 2.11b)) is described by the Bragg law that relates the wavelength of the X-rays to the interatomic spacing, and is given by the following equation:

$$2d \sin(\theta) = n\lambda \quad (2.13)$$

where d is the perpendicular distance between pairs of adjacent planes, θ is the angle of incidence or Bragg angle, λ is the wavelength of the beam (1.54 \AA for a copper tube source), and n denotes an integer number, known as the order of the reflection and is the path difference, in terms of wavelength, between waves scattered by adjacent planes of atoms.

XRD can provide additional information regarding the crystallite size. The average crystallite size can be calculated by the peak broadening of the diffraction peaks using the Scherrer equation:

$$t = \frac{K\lambda}{\beta \cos(\theta)} \quad (2.14)$$

where t is the crystallite size, β is the full width at half of the maximum intensity of the reflection peak, and K is the Scherrer constant. XRD is in general useful for nanoscale crystallites with diameters below 100–200 nm since peak broadening is negligible for bigger particles⁶¹.

2.7.4 X-Ray Photoelectron Spectroscopy (XPS)

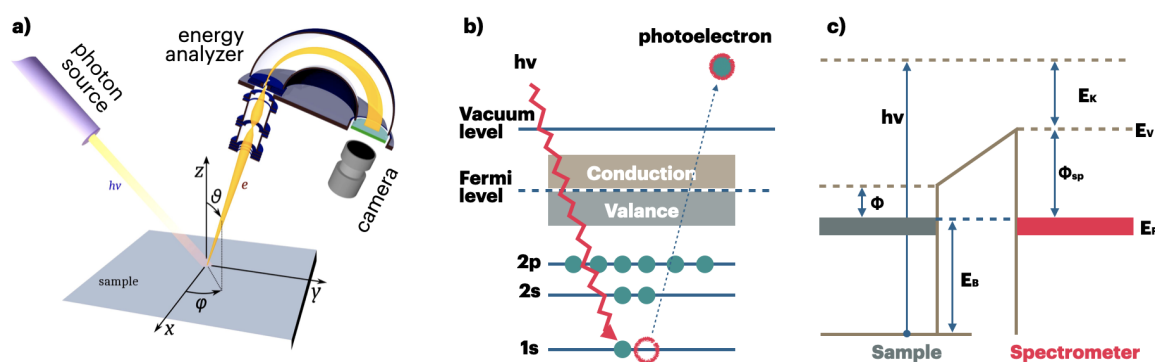


Figure 2.12: a) Schema angle-resolved photoemission spectroscopy. Adapted from, Ref.⁶². b) and c) Schematic illustration of the principle behind XPS by energy level diagram. (Adapted from Ref.⁶³)

X-ray photoelectron spectroscopy (XPS) is one of the most preferred tools that provides the chemical composition of material surfaces within 10 nm, along with elemental information and detection sensitivity of 0.1-1 at.% for all the elements except H and He⁶⁴. XPS is a potent nondestructive surface-sensitive technique that allows to investigate the surface chemistry of nanoparticles, nanostructured materials, surfaces, coatings, and thin films⁶³.

XPS operates under ultra-high vacuum conditions, exposing the material to X-rays. Photoelectrons are ejected from different energy levels of the material's surface atoms if the provided energy is high enough to overcome the work function of the solid. These photoelectrons are subsequently detected by a hemispherical analyzer that measures their kinetic energy ($E_{kinetic}$). A schematic of this process is shown in Fig. 2.12a. A variation in the binding energy ($E_{binding}$), relative to the Fermi level (Fig. 2.12b and c), occurs in an electron at a specific energy level of an element. This shift, known as a chemical shift, results from changes in the element's oxidation state or the electronic charge distribution around its nucleus due to alterations in the chemical bonding or its surrounding environment⁶⁴. The binding energy of electrons can be determined from their kinetic energy using the equation^{61,64}:

$$E_{binding} = E_{photon} - (E_{kinetic} + \Phi) \quad (2.15)$$

where E_{photon} is the X-ray photon energy and Φ is the work function of the electron energy analyzer.

The photoemission process can be conceptualized in three steps:

1. Initial state effects: The molecule absorbs the photon, transferring its energy to the molecule's electrons, which become excited.
2. Final state effects: The excited electron moves to the molecule's surface. During this journey, it may or may not collide with other particles.
3. Extrinsic effects: Excited electrons that do collide with particles lose energy. Subsequently, the excited electron escapes the molecule's surface into the vacuum, where it is detected.

The binding energy spectrum, reflects unique patterns for different elements, and variations in binding energy can be attributed to changes in oxidation state and chemical environment. This enables the identification of elements and their oxidation states, while quantitative elemental information is derived from peak measurements or integrated peak areas.⁶¹

2.7.5 Scanning X-ray induced secondary electron images (SXISE)

Another feature of the PHI Versaprobe II XPS is the scanning X-ray induced secondary electron images (SXISE), which is generated by scanning a focused sub-10 μm X-ray beam across the sample. In conventional scanning electron microscopy (Scanning electron microscopy (SEM)), secondary electrons are crucial for revealing sample morphology and topography. They produce high-resolution images that expose details at the 1-5 nanometer scale. These secondary electrons originate from the surface layers of the sample, creating images that highlight surface features. Edges, peaks, and fine structures appear brighter due to the ease of electron escape from these areas⁶⁵. Similar to SEM, SXISEs in XPS enable the acquisition of high-resolution images and real-time navigation to areas of interest for analysis. SXISE images offer 100% confidence in locating small features of interest and in avoiding areas with contamination and inhomogeneities during analysis⁶⁶.

2.7.6 Thermogravimetric analysis (TGA)

Thermogravimetric analysis (TGA) works by monitoring the mass changes of a sample under specific conditions, focusing mainly on phenomena related to heat such as absorption, adsorption, desorption, vaporization, sublimation, decomposition, oxidation, and reduction⁶⁷. This method is useful in studying volatile or gaseous substances released during chemical reactions across various materials, including nanomaterials, polymers, and fibers. Additionally, TGA facilitates the prediction of thermal stability and enables the examination of reaction kinetics by adjusting factors like sample weight, volume, physical form, and atmospheric conditions, although it cannot analyze phenomena like melting and crystallization behaviors.

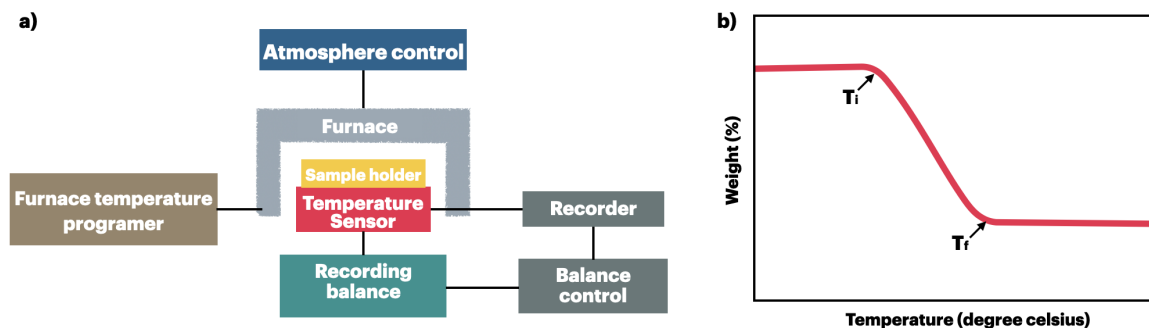


Figure 2.13: a) Schematic representation of a thermobalance and b) typical thermogravimetry curve. Adapted from, Ref⁶⁷

The instrument employed in thermogravimetry (TG) is referred to as a thermobalance. The fundamental components of a standard thermobalance are depicted in a simple block diagram in Fig. 2.13a and are outlined below:

- Balance: microbalance, record the changes
- Furnace: linear heating rate can be achieved
- The sample holder: crucible
- Temperature Programmer: recorded in degrees per minute in terms of the Kelvin or Celsius scale
- Recorder: automatic recording unit for the mass and temperature

During TG, a substance is subjected to either uniform heating or maintained at a constant temperature, resulting in the generation of a continuous plot known as the thermogravimetric curve, shown in Fig. 2.13b. This curve typically illustrates mass reduction along the y – $axis$ and temperature increase along the x – $axis$, aiding in the assessment of sample purity and the understanding of transformation modes within specific temperature ranges⁶⁸. In a TG curve depicting single-stage decomposition, two critical temperatures are observed: the initial T_i and the final temperature T_f . T_i signifies the temperature at which the onset of mass change is observed, while T_f indicates the completion of the decomposition process.

Chapter 3

Motivation

3.1 Problem Statement

Despite the significant potential of CNS in nanocomposites, the widespread adoption of this technology is limited by poor dispersion quality². CNTs and graphene, owing to their stable sp^2 hybridization, exhibit chemical inertness and are incompatible with many solvents. Achieving effective inclusion of these materials into cement concrete mixes requires a thorough optimization of dispersion procedures². To overcome this challenge, extensive research has been conducted on surface modifications to enhance the surface functionality of CNS. Various techniques, including physical dispersion and chemical methods such as covalent and non-covalent functionalization, have been explored for achieving optimal dispersion⁸⁻¹¹.

In the physical method, high-energy ultrasound and overspeed centrifugation are used to disperse CNS⁸. However, this approach may result in fragmentation of CNS, reducing their aspect ratio and damaging their structure. Furthermore, maintaining stability of the dispersion is challenging because CNS tend to re-aggregate over time due to VdW forces¹⁰.

The chemical covalent functionalization method involves treating CNTs with strong acids like concentrated H_2SO_4 or HNO_3 , which destroys the end caps of the tubes and introduces surface defects where various active functional groups ($-COOH$, $-OH$) are attached⁵². In contrast, the non-covalent approach adds surfactants to the CNT structure through adsorption⁶⁹. This process involves additional reagents and a multi-step procedure, making it challenging for large-scale production and practical implementation

Both methods require a preliminary dispersion for their application, which is particularly challenging in the cement industry, where the product is sold as a powder. Therefore, in this work, we propose an alternative route to introduce/disperse CNS directly into the cement matrix. Two routes are proposed: one involves the direct growth of CNS in the cement matrix *via* CVD, and the second involves integrating CNS through ball milling.

3.2 General and Specific Objectives

3.2.1 General Objectives

The primary aim of this study is to directly introduce/disperse CNS into the cement matrix, with a focus on enhancing the mechanical properties of the nano-engineered cement, specifically its flexural strength. This will be achieved through two distinct methods: firstly, by growing CNS directly in the cement matrix *via* CVD, and secondly, by dispersing CNS through ball milling.

3.2.2 Specific Objectives

- **Synthesis and Characterization of Nanostructured Materials:** This objective involves investigating and meticulously characterizing glucose-derived CNS synthesized through evaporation and pyrolysis using CVD techniques. Advanced analytical tools such as Raman spectroscopy XRD will be employed to delve into the intricate structural and chemical properties of the synthesized materials.
- **Integration of CNS into Cement Matrix:** The focus here is on incorporating the synthesized CNS into cement matrices using versatile techniques such as CVD and ball milling. The efficacy of each integration method in achieving optimal dispersion and functionalization of the nanostructures within the cement matrix will be evaluated. Characterization techniques including Raman spectroscopy, XRD, and XPS will provide insights into the effectiveness of these integration methods.
- **Evaluation of Nano-engineered Cement Performance:** This objective entails a comprehensive evaluation of nano-engineered cement composites, covering mechanical strength, durability, and permeability. Mechanical tests, including compression and flexural strength assessments, will be conducted to gauge the structural integrity and load-bearing capacity of the composites. Additionally, water infiltration evaluations will be performed to assess the resistance against fluid infiltration, ensuring long-term durability in practical applications.

Chapter 4

Methodology

4.1 Materials and Equipment

4.1.1 Materials

- Glucose P.A. $C_6H_{12}O_6 \cdot H_2O$ (glucose)
- Cement Guapan (CG)
- Iron Chloride reagent grade 97% ($FeCl_3$)
- NC3100™ Research grades - Thin MWCNT 95+%C purity (CNT(NC))
- Multi-walled Carbon nanotube produced at Yachay Tech University (CNT(YT))
- Distilled water
- Sand

4.1.2 Equipment

The main equipment's used for nano-engineered cement synthesis, shown in Fig. 4.1, are:

1. Vibratory sieve shaker (AS 200 BASIC)
2. Mixer mill (MM 500 NANO)
3. Balance (Boeco Germany)
4. CVD (OTF-1200X)
5. Cubic $1 \times 1 \times 1 \text{ cm}^3$ and rectangle $6 \times 1 \times 1 \text{ cm}^3$ molds

6. Common blender

7. Alumina boats (80 ml and 1.25 ml)

Additionally, a very common lab equipments such as Beakers, Test tube, micro spatula, hot plate, etc. were used.



Figure 4.1: Main equipment's used for the synthesis of nano-engineered cement and for specimen preparation

4.2 Synthesis of glucose-derived nanostructure

Before attempting to incorporate a specific type of carbon nanostructure into the cement matrix through the mixture of cement and glucose, we conducted an initial investigation on the glucose-based product using two distinct approaches.

Firstly, a multi-layer graphene-type carbon nanostructure was synthesized using glucose as a carbon source (Fig. 4.2 path a). For this synthesis, 0.15 g of glucose was placed in a small alumina boat and subjected to calcination treatment in a tube furnace at 800 °C for 1 h under an argon flow of 30 mLmin⁻¹. Subsequently, the furnace was cooled down to room temperature under an argon flow, and the resulting material was labeled as g(800°C). It is crucial

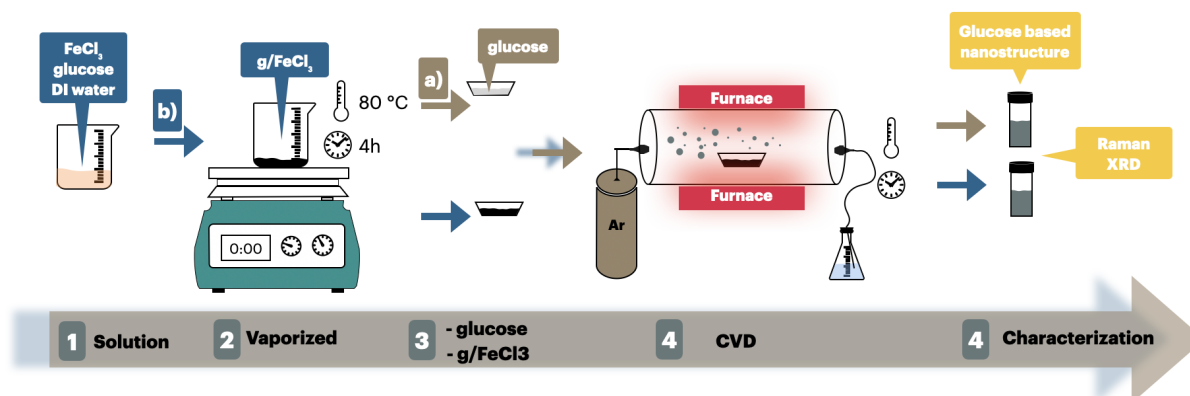


Figure 4.2: Synthesis methods of multi-layer graphene. In path a, glucose is subjected to carbonization treatment in a tube furnace. In path b, glucose is mixed with iron chloride and subjected to vaporization and carbonization treatment.

to emphasize that this calcination treatment is a common step in all the CVD methods described below and will be denoted as the calcination treatment (Calcination treatment (CT))*.

Furthermore, a few layers of graphene were synthesized via CVD, adapting the methodology proposed by Zhang et al.⁷⁰ as depicted in Fig. 4.2 path b. In a 50 mL beaker, 2 g of glucose and 2 g of $FeCl_3$ were dissolved in 5 mL of distilled water. The solvent of the yellow-colored solution was evaporated at 80 °C on a hot plate for 4 hours, resulting in a black solid powder ($g@FeCl_3$). Subsequently, 0.15 g of $g@FeCl_3$ was placed in a small alumina boat and underwent CT at 800 and 1,000 °C for 1 hour and 30 minutes, respectively, and the resulting material was labeled as $gFe(800^\circ C)$ and $gFe(1000^\circ C)$. For simplicity, the last was labeled as Multi-layer graphene (MLG) (multi-layer graphene). Both samples, underwent Raman spectroscopy to assess the quality of graphitization.

4.3 Synthesis of nano-engineered cement

CVD

The procedure for synthesizing nano-structured cement *via* CVD and milling is depicted in Fig.4.3. In both methods, the initial step involved subjecting the cement to a vibratory sieve with a 45 μm filter. For the CVD method, 0.5 wt% glucose was mixed with cement using a blender for 5 minutes. Subsequently, 15 g of the resulting solid mixture was placed in an alumina boat and introduced into the furnace tube for CT at 800 and 1000 °C, as depicted in Fig.4.3 path a. The resulting samples were labeled as $g/CG - L$ and $g/CG - H$. This same procedure was repeated, replacing glucose with $g@FeCl_3$, and the obtained products were labeled as $gFe/CG - L$ and $gFe/CG - H$.

*CT: Material introduced into a tube furnace and subjected to calcination at 800 °C for 1 h or 1000 °C for 30 minutes under an argon flow of 30 mL/min, followed by cooling to room temperature under the same argon flow.

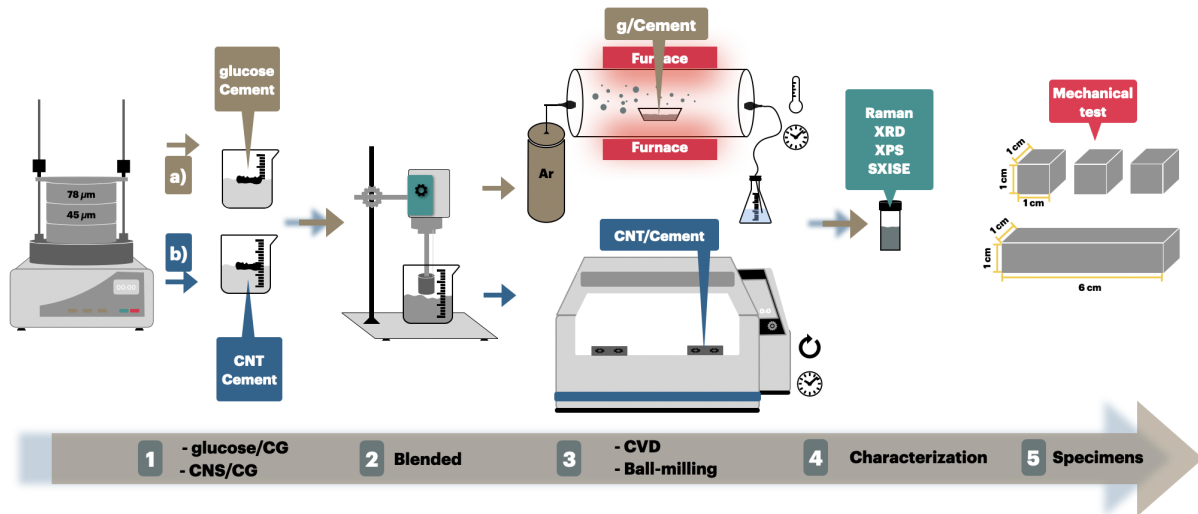


Figure 4.3: Synthesis methods to produce nano-engineered cement. Path a illustrates the steps taken to produce nano-engineered cement *via* CVD, while path b represents the process through ball milling.

Ball milling

In this approach, the nano-structured cement was synthesized by blending cement with 0.5 wt% of *CNTs* (Fig.4.3 path b) for 5 min. Subsequently, 16 g of the mixture and 40 g of very small stainless steel balls were placed in the grinding jar and milled for 3 hours, with 5 min at 25 Hz and 1 min at 0 Hz intervals to prevent overheating. The resulting product was labeled as *CNT(NC)/CG*. The same procedure was replicated, with *CNT(YT)* and *MLG*, and the obtained products were labeled as *CNT(YT)/CG* and *MLG/CG*.

The byproducts mentioned above are summarized in Table 4.1.

4.4 Specimen preparation

Due to the limited quantity of modified cement obtained, the specimens for mechanical tests were fabricated as small as possible, following the dimensions used by Liebscher et al.⁷¹. The fabrication procedure is illustrated in Fig. 4.4. To prepare the specimens, 14 g of nano-engineered cement and 56 g of sand were thoroughly mixed in a 250 mL beaker. Subsequently, 18 mL of deionized water was added and immediately mixed to form a viscous paste. The paste was then poured into oiled steel molds to cast cubes and beams with dimensions of $10 \times 10 \times 10 \text{ mm}^3$ and $10 \times 10 \times 60 \text{ mm}^3$, respectively. The nanocomposites were cured under laboratory conditions at approximately 23°C . After 14 days, the samples were stored in an oven at 60°C overnight before undergoing mechanical testing.

Code	Carbon nanostructures			wt%	Cement
	Temperature ($^{\circ}C$)	Time (min)	C source		
$g(800^{\circ}C)$	800	60	glucose		
$gFe(800^{\circ}C)$	800	60	$g/FeCl_3$		
$gFe(1000^{\circ}C)[MLG]$	1000	30	$g/FeCl_3$		
CVD					
	Temperature ($^{\circ}C$)	Time (min)	C source	wt%	Cement
$g/CG - L$	800	60	glucose	0.5	CG
$g/CG - H$	1000	30	glucose	0.5	CG
$gFe/CG - L$	800	60	$g/FeCl_3$	0.5	CG
$gFe/CG - H$	1000	30	$g/FeCl_3$	0.5	CG
Ball milling					
	Frequency (Hz)	Time (h)	C structure	wt%	
MLG/CG	25	3	MLG	0.5	CG
$CNT(NC)/CG$	25	3	$CNT(CC)$	0.5	CG
$CNT(YT)/CG$	25	3	$CNT(YT)$	0.5	CG

Table 4.1: Summary of carbon nanostructure and nano-engineered cement composites produced *via* CVD and ball milling methods.

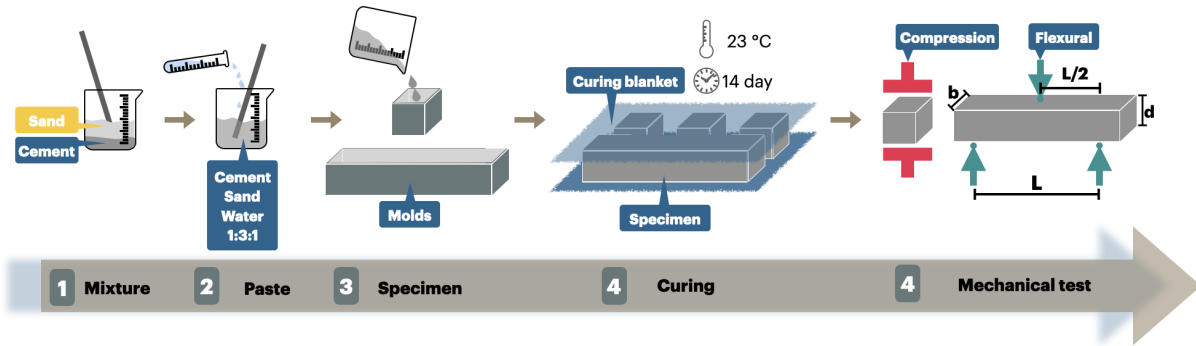


Figure 4.4: Illustrates the process followed to prepare the specimens for mechanical tests.

The compressive strength (E) was calculated from the stress (σ) vs. strain (ϵ) diagrams using the formula:

$$E = \text{slope} = \frac{\sigma}{\epsilon} \quad (4.1)$$

The flexural strength was measured using three-point bending with a span length (L) of 40 mm and a support span of $L/2$ (20 mm), following ASTM Standards C1161. The standard formula for the flexural strength (S) of a

beam in three-point bending is given by:

$$S = \frac{3PL}{2bd^2} \quad (4.2)$$

where: P = break force, L = outer (support) span, b = specimen width, and d = specimen thickness.

4.5 Characterization

The nano-engineered cement was characterized using the equipment shown in Fig. 4.5. The type of carbon nanostructure was analyzed using Raman spectroscopy with a HORIBA LabRam spectrometer using 633 nm excitation wavelength. The phase changes in the cement were examined through X-ray diffraction (XRD) analysis, which was performed using a RIGAKU MINIFLEX 600 X-ray diffractometer operating at 40 kV and 15 mA with $CuK(\alpha)$ radiation. The chemical composition was assessed using X-ray photoelectron spectroscopy (XPS) with a PHI 5000VersaProbe III X-ray photoelectron spectrometer. The SEM feature in XPS was utilized to study the surface topology. Thermogravimetric analysis was conducted using a TG instruments TGA55 instrument in an inert atmosphere at a heating rate of 10 °C/min until 900°C. Finally, the mechanical properties of the product were evaluated using a United Testing DFM Series Floor Model Universal Test Machine (UTM) at a preloading rate of 0.5 and a testing to failure rate of 0.2.



Figure 4.5: Equipment's used for characterization.

Chapter 5

Results & Discussion

5.1 Glucose based nanostructures

5.1.1 Raman spectroscopy and XRD

Raman spectroscopy (Fig. 5.1a) was employed to trace the evolution of glucose-derived materials. The initial spectrum showcases the characteristic vibration of glucose, as previously noted by Zhang et al.⁷². The subsequent spectra (*glucose/g@FeCl₃*), corresponding to glucose mixed with iron chloride evaporated at 80 °C, comprise two broad overlapping bands known as the D and G bands. The D band, at approximately 1350 cm^{-1} , is attributed to ring-breathing vibrations in benzene rings, indicating defects in graphitic lattices. The G band, located at approximately 1580 cm^{-1} , involves the in-plane bond-stretching motion of pairs of C sp^2 atoms⁷³. The spectra obtained exhibit typical features of carbonized materials, as commonly reported for hydrochar^{74,75}. Additionally, the spectra indicate the presence of iron species at a lower Raman shift. Moving to the subsequent two spectra, *g(800°C)* and *gFe(800°C)*, which represent pyrolyzed glucose and glucose mixed with iron chloride, both exhibit three distinct and prominent features indicative of well graphitized CNS: the D, G, and 2D bands located at 1326, 1582, and 2661 cm^{-1} , respectively. Here, the 2D band arises from a two-phonon process involving scattering of two phonons near the K-point. These phonons are associated with the vibrations of carbon atoms in the graphene lattice⁵⁸. The intensity ratio of G and D bands, denoted as (I_G/I_D), serves as an indicator of the crystalline degree of CNS, with values of 1 for *g(800°C)* and 0.86 for *gFe(800°C)*⁵⁸. The reduced intensity in *gFe(800°C)* suggests a diminished presence of defective sites in the lattice. In the subsequent spectrum, *gFe(1000°C)*, there is a further reduction in the intensity ratio (0.78) and in the Full width at half maximum (FWHM) of the 2D peak, indicating an improvement in surface quality and a reduction in layers within CNS⁵⁷, respectively.

These findings indicate that at 1000 °C, there is a further thermal decomposition and rearrangement of carbon atoms. This process, known as graphitization, results in the creation of well-ordered sp^2 -hybridized carbon structures typical of graphene, achieved by the removal of heteroatoms and functional groups. Furthermore, iron species can serve as catalysts in these reactions, facilitating the graphitization process and amplifying the formation of ordered

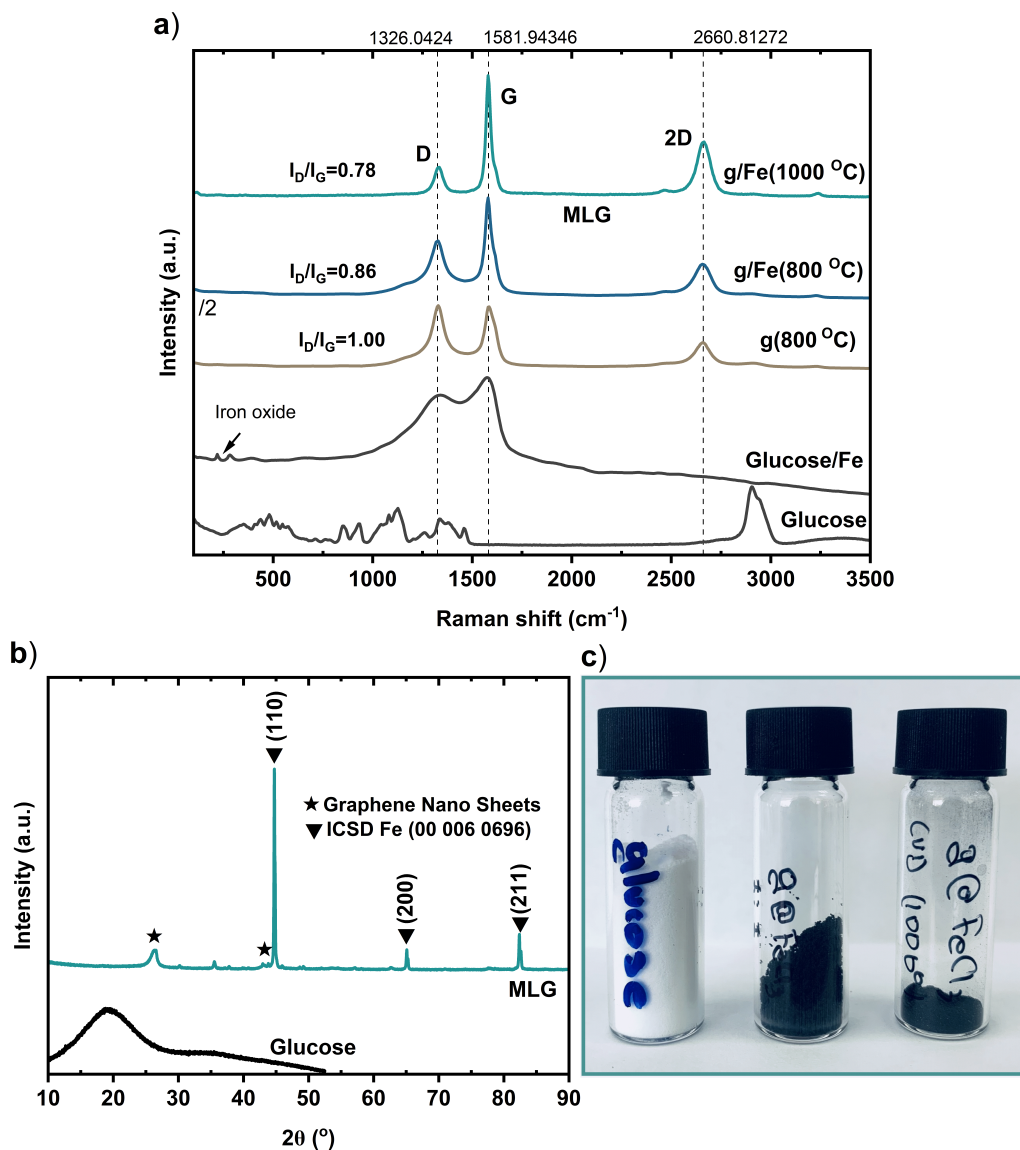


Figure 5.1: Illustrates glucose-derived materials: a) Raman spectra of glucose and glucose subjected to various treatments, b) XRD of glucose and MLG, and c) optical image of the materials.

carbon structures that resemble graphene⁷⁶. For simplicity, we label *gFe(1000°C)*, demonstrating the characteristic vibration of multilayer graphene, as MLG.

The chemical composition and phase structure of glucose and MLG were examined using X-ray diffractograms

and Inorganic Crystal Structure Database (ICSD) cards, as depicted in Fig. 5.1b. In the glucose diffractogram, a characteristic amorphous broad reflection is observed around $2\theta = 20^\circ$. In contrast, the MLG diffractogram exhibits a distinct reflection (highlighted with a star) at 26.2° , which corresponds to the (002) plane of graphitic carbon⁷⁰. Additionally, the diffractograms reveal peaks (indicated by triangles) at 44.7 , 65.0 , and 82.3° , corresponding to *Fe* (ICSD 00-006-0696) and representing the (110), (200), and (211) crystalline planes, respectively. The sharp and pronounced profile of these peaks suggests the formation of well-crystallized *Fe* nanoparticles⁷⁰.

The combined results from Raman spectroscopy and XRD suggest that glucose, when mixed with iron chloride and subjected to pyrolysis at 1000°C , yields higher-quality CNS materials. Finally, Fig.5.1c illustrates both the precursor and by product of CNS.

5.2 Nano-engineered cement

5.2.1 Raman

CVD

Following the development of a suitable synthesis process for CNS, the next phase involved integrating them into the cement matrix using CVD (see Fig. 5.2c). Fig. 5.2a shows the Raman spectra of cement and nano-engineered cements. The cement spectra display three peaks at 500 - 800 , 852 , and 1079 cm^{-1} which correspond to C_3A , $\text{C}_3\text{S}/\text{C}_2\text{S}$, and gypsum, respectively, with $\text{C}_3\text{S}/\text{C}_2\text{S}$ being more prominent⁷⁷. The next two spectra, *g/CG - L* and *g/CG - H*, indicate pure glucose mixed with cement. Both exhibit three different features of graphitized CNS: the D, G, and 2D bands located at 1333.7 , 1595 , and 2651 cm^{-1} , respectively, alongside the cement vibration mode⁷⁸. Similarly, the next two spectra, *gFe/CG - L* and *gFe/CG - H*, which show glucose combined with iron chloride and then mixed with cement, exhibit the three characteristics of graphitized CNS, alongside the cement vibration mode. The inset image shows the particular places where Raman measurements were taken. Notably, the cement appears as white dazzling bubbles, whereas the composite provides the impression that white cement bubbles are covered by a gray material, indicating the presence of CNS. The intensity ratio in Fig. 5.2b decreases from 1.06 for *g/CG - L* to 1.03 for *g/CG - H*, and from 1.03 for *gFe/CG - L* to 1.00 for *gFe/CG - H*. This trend suggests a reduction in defects within the CNS as the temperature increases from 800 to 1000°C , indicating a higher quality of CNS is obtained⁵⁸.

In summary, Raman spectra analysis reveals the successful incorporation of graphitized carbon nanostructures into cement matrix using CVD. The distinct D, G, and 2D bands, as well as a decrease in intensity ratio with increasing temperature, suggest that the carbon nanostructures are of higher quality. These findings demonstrate the efficacy of the synthesis method and CVD procedure.

Ball Milling

In this stage, the incorporation of CNS into the cement matrix was achieved through the ball milling process (see Fig. 5.3d). Fig. 5.3a, b and c shows the Raman spectra of cement, CNS, and nano-engineered cements. The

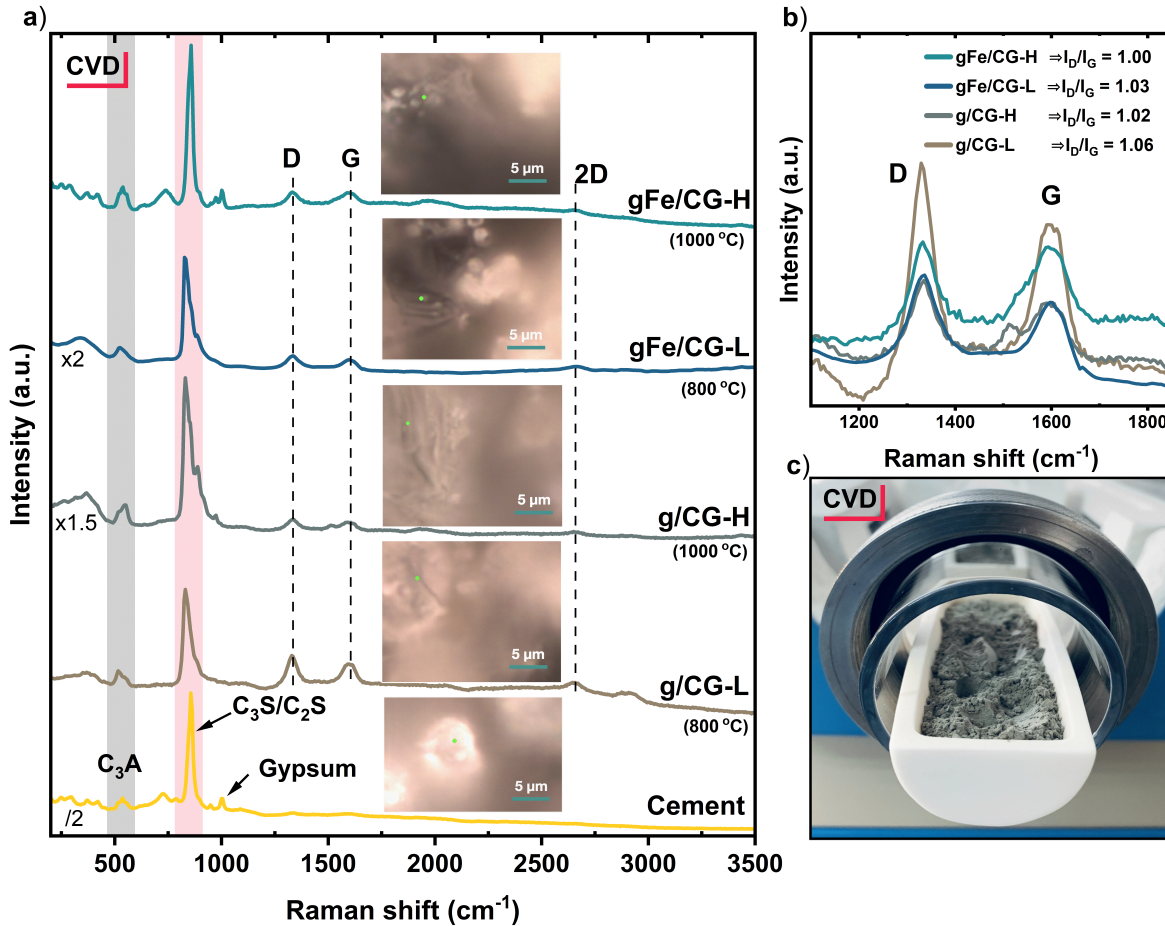


Figure 5.2: Illustrates the synthesis of nano-engineered cement *via* CVD. a) Raman spectra of plain cement and nano-engineered cement, displaying the three characteristic graphitized CNS modes: the D, G, and 2D, alongside the cement vibration mode, C_3S/C_2S . b) Intensity ratio of D and G bands, indicating the material quality. c) Optical image of the mixture being introduced into CVD.

cement spectra, also plotted in the CVD graphs, is included for illustrative purposes. The second spectra, Fig. 5.2a illustrating MLG, reveal the three distinct characteristics of CNS: the D, G, and 2D bands positioned at 1333.1, 1579.5, and 2666 cm⁻¹, respectively, with an I_G/I_D ratio of 0.53. The following spectrum, *MLG/CG*, exhibits MLG characteristics alongside the vibrations of the cement, with an I_G/I_D ratio of 0.90. The increased intensity implies the formation of certain defects, suggesting a certain degree of functionalization of GML with cement⁶⁰. The inset figure shows MLG, around 3 μm, apparently surrounded by cement particles.

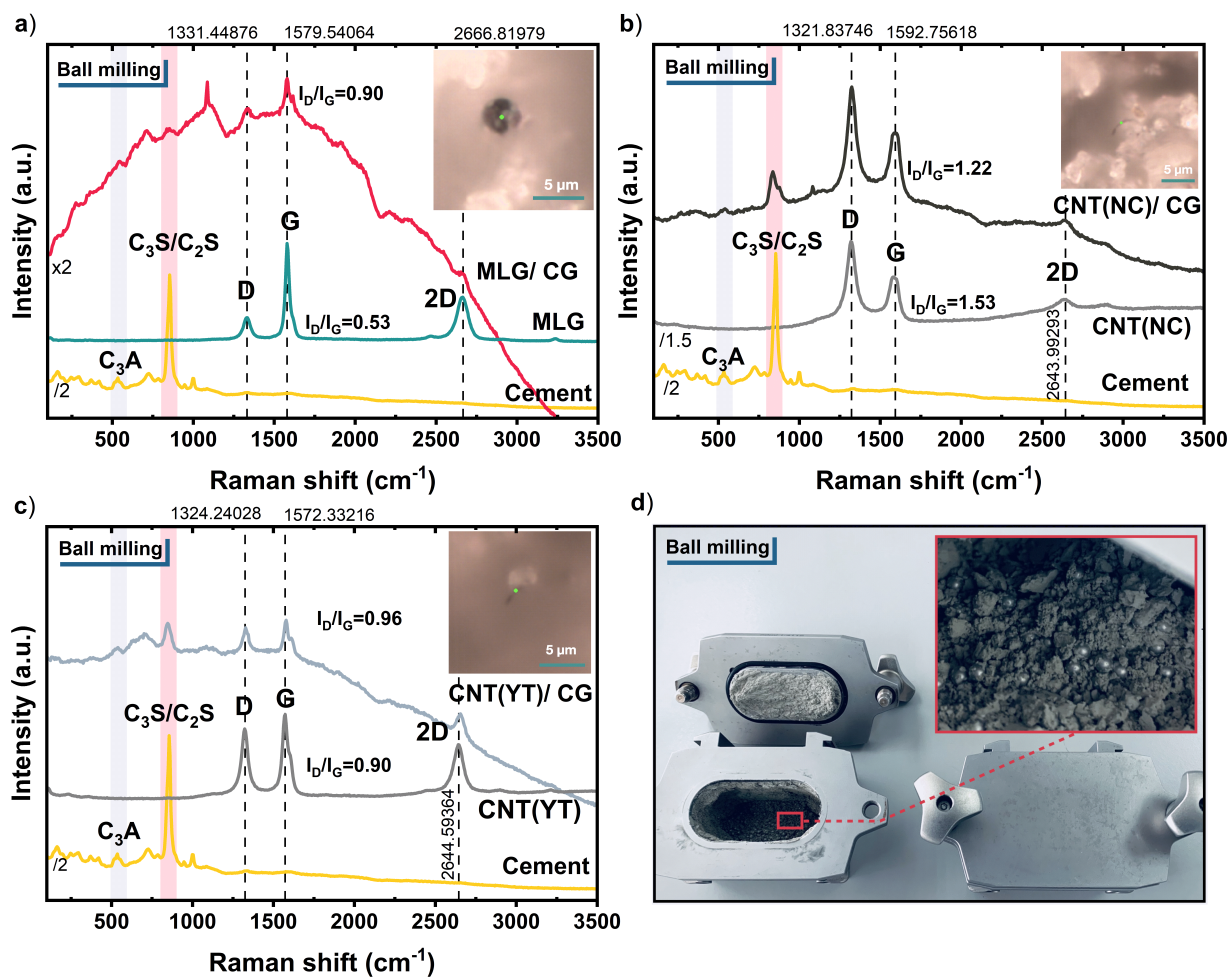


Figure 5.3: Illustrates the synthesis of nano-engineered cement through Ball milling. a, b, and c) show the Raman spectra of plain cement and nano-engineered cement produced with MLG, CNT(NC), and CNT(YT), respectively. The composite spectra display the three characteristic graphitized CNS modes: the D, G, and 2D, alongside the cement vibration mode, C_3S/C_2S . d) Shows an optical image of the mixture after ball milling treatment.

Continuing, in the second spectra, depicted in Fig. 5.3b, the Raman spectra of *CNT(NC)* exhibit three distinct characteristics: the D, G, and 2D bands positioned at 1321.8, 1592.7, and 2644 cm⁻¹ respectively, with an I_G/I_D ratio of 1.53. The following spectrum, representing the composite *CNT(NC)/CG*, exhibits *CNT(NC)* characteristics alongside the vibrations of the cement, with an I_G/I_D of 1.22. The decrease in intensity ratio may be attributed to the separation or disentanglement of CNT agglomerates. This hypothesis is supported by the inset figure in Fig. 5.3b

where an isolated single CNT(NC) of around $4\ \mu\text{m}^*$ can be observed.

Similarly, in Fig. 5.3c, the CNT(YT) spectra reveal the D, G, and 2D bands located at 1324.2 , 1572.3 , and $2644\ \text{cm}^{-1}$ respectively, with an I_G/I_D of 0.90 . The subsequent spectra, $\text{CNT(YT)}/\text{CG}$, display CNT(YT) vibrations alongside those of the cement, with an I_G/I_D of 0.96 . The slight increase in intensity suggests a certain degree of functionalization of CNT(YT) with cement. The inset figure depicts CNT(YT) particles, around $2\ \mu\text{m}$, seemingly embedded in cement particles.

During these processes, ball milling generates shearing forces through high-energy collisions between grinding balls and particles. As CNS agglomerates undergo intense shearing forces, the VdW forces holding them together are overcome, leading to their disintegration and dispersion within the cement matrix. Throughout this process, CNS, subjected to repeated impacts and shear forces, are broken down into smaller sizes, and surface defects are introduced, facilitating functionalization with cement.

In summary, Raman spectra analysis reveals the successful dispersion and functionalization of GML and CNT(YT) into and with cement matrix.

5.2.2 XRD

CVD and Ball milling

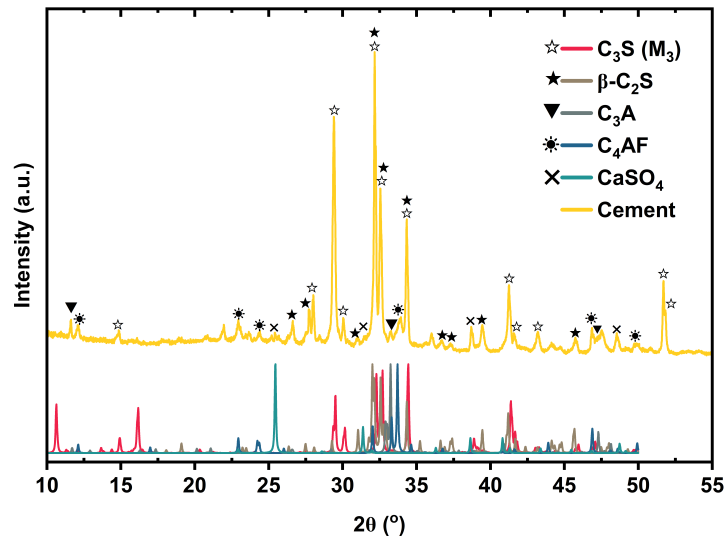


Figure 5.4: XRD patterns of cement and its components extracted from the Inorganic Crystal Structure Database, labeled as C_3S (white star), C_2S (black star), C_3A (triangle), C_4AF (asterisk), and CaSO_4 (cross).

*Nanocyl NC7000 multi-walled carbon nanotubes: length $0.1\text{-}10\ \mu\text{m}$

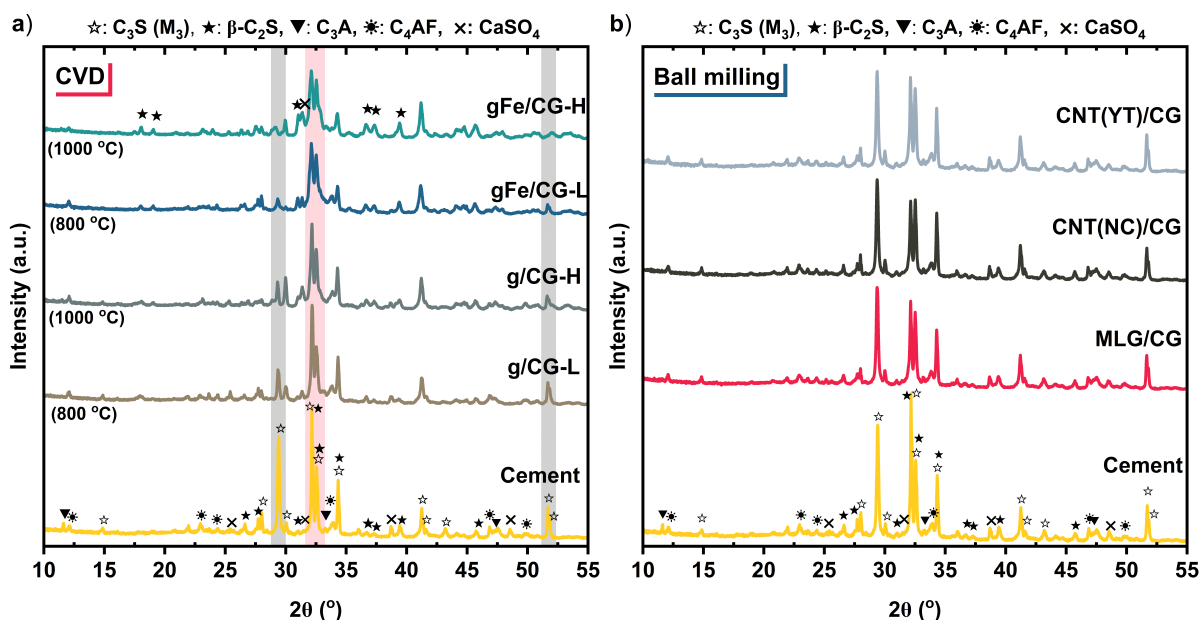


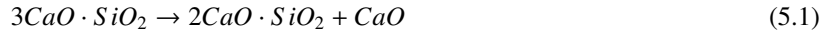
Figure 5.5: XRD patterns of plain cement and nano-engineered cement synthesized: a) via CVD, and b) through ball milling.

The XRD patterns illustrated in Fig. 5.4 depict the crystalline composition of cement and its components extracted from the ICSD. The crystal phases utilized include C_3S (ICSD 64759), C_2S (ICSD 81096), C_3A (ICSD 100220), C_4AF (ICSD 9197), and $CaSO_4$ (ICSD 16876)⁷⁹. These patterns reveal that the dominant crystalline phases present in cement spectra are alite, belite, aluminate, and ferrite, as evidenced by the diffraction angles of the most intense peaks, aligning with the primary constituents of clinker. The presence of the alite monoclinic M3 polymorph in the cement is indicated by peaks found at specific diffraction angles of 29.5 , 32.2 , 32.6 , 34.4 , 41.3 , and 51.7° . Regarding belite, most prominent peaks coincide with the alite phase, except for specific peaks occurring at $2\theta = 41.25^\circ$, indicating the presence of the β - C_2S polymorph, prized for its hydraulic characteristics⁸⁰. Additionally, the aluminate orthorhombic key diffraction peak is located at $2\theta = 32.95^\circ$, while ferrite's key diffraction peaks are situated at $2\theta = 12.1^\circ$ and 33.7° ⁸⁰.

Figure 5.5a depicts the XRD diffractograms of nano-engineered cement synthesized *via* CVD. The diffractograms for *g/CG-L* and *g/CG-H* exhibit a significant reduction in the alite peak at 29.41° , highlighted with gray bar, as the temperature increases, a trend that becomes more pronounced for *gFe/CG-L* and nearly eliminates the peak for *gFe/CG-H*. Furthermore, the subsequent peaks at 32.2° and 32.6° , highlighted with red bar, corresponding to both alite and belite, show a reduction in intensity with increasing temperature and the addition of *Fe*. This trend extends to the alite peak at 51.7° , highlighted with gray bar. Alongside the intensity reduction, the peaks tend to

broaden, indicating a loss of crystallinity in the material. The final diffractogram indicates a reduction or destruction of some alite phases, while certain belite peaks remain relatively unchanged and new belite peaks appear.

These observations suggest a transformation from alite to belite, a phenomenon described by Carlson⁸¹ and represented by the equation:



According to Schraut et al.⁸², tricalcium silicate remains stable above $1250 \pm 25^\circ C$ in thermodynamic equilibrium. Below this temperature, it decomposes into dicalcium silicate and CaO , and the rate of decomposition is temperature-dependent. Conversely, Tenório et al.⁸³ demonstrated that incorporating 0.8% iron oxide into pure alite can significantly increase the amount of decomposed C_3S by up to 48%. This indicates that the addition of iron oxide to alite catalyzes the nucleation of CaO and C_2S at the surface of the C_3S crystals, thereby enhancing decomposition kinetics.

These findings suggest that the primary crystalline phase of cement, alite, undergoes thermal degradation with increasing temperature. The presence of iron nanoparticles exacerbates this degradation due to their catalytic activity. Consequently, when exposed to higher temperatures, the cement structure undergoes alterations and loses its intended qualities, given the critical role of this phase in strength development⁸⁴.

Moving to Fig. 5.5b, the XRD diffractograms of nano-engineered cement synthesized via ball milling are displayed. Despite a slight reduction in the peaks at 32.2° and 32.6° , corresponding to both alite and belite, observed in MLG/CG , $CNT(NC)/CG$, and $CNT(YT)/CG$, there are no significant alterations in the diffractograms. This suggests that the ball milling method does not induce substantial changes in the cement composition beyond this minor reduction in peak intensity, which is consistent with some studies with graphene oxide incorporation⁸⁵.

5.2.3 TGA

To further investigate the thermal transition of alite to belite, thermogravimetric analysis was performed on plain cement, as depicted in Fig. 5.6. The plain cement sample initially experiences weight losses of 0.7% and 0.5% at 56 and 120 °C, respectively, attributed to gypsum. The subsequent weight loss of 0.5% at 400°C is attributed to portlandite⁸⁶. The decomposition temperature of the carbonated phase (derived from $CaCO_3$) was approximately 625 °C, as determined by the differential weight. Notably, no further weight loss is observed beyond this temperature range. The recorded weight loss of 5.2% at this temperature corresponds to the decomposition of $CaCO_3$ into CaO and CO_2 ⁸⁷. This observation corroborates and reinforces the findings obtained from X-ray Diffraction analysis.

Samples

Fig. 5.7 illustrates the cement and nano-engineered cement produced *via* CVD and ball milling. The thermally treated samples exhibit a color change from gray to cream-like, suggesting the decomposition of carbonate aggregates into CaO and CO_2 , leading to a brighter appearance associated with the whitish tint of lime, as described by Hager⁸⁸. Additionally, they appear more compacted. In contrast, the ball milling samples do not display any color change. Instead, they exhibit a more sponge-like feature, indicative of the presence of CNS.

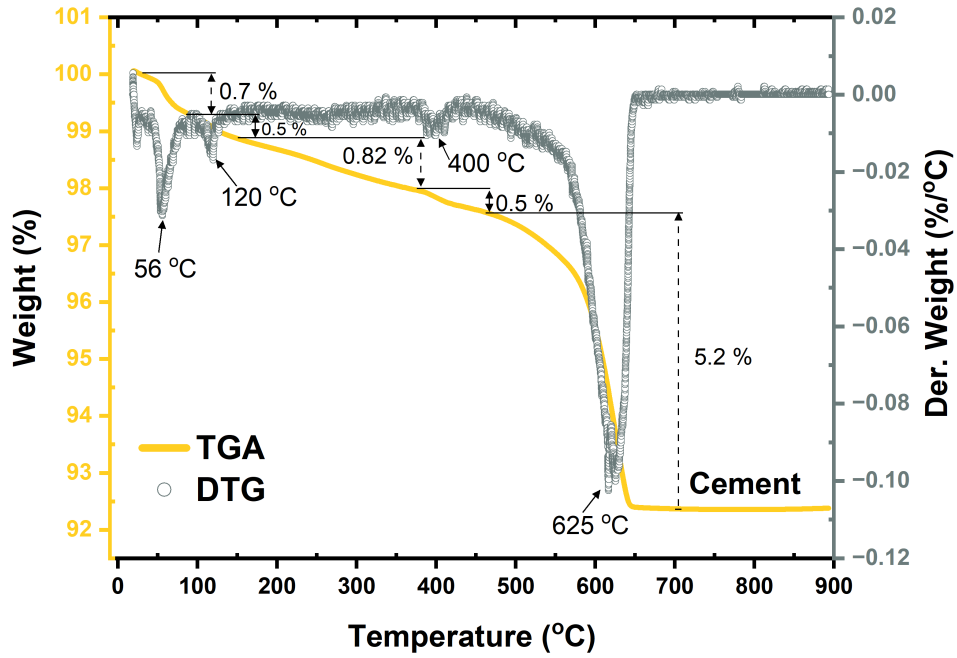


Figure 5.6: Thermogravimetric curves of plain cement

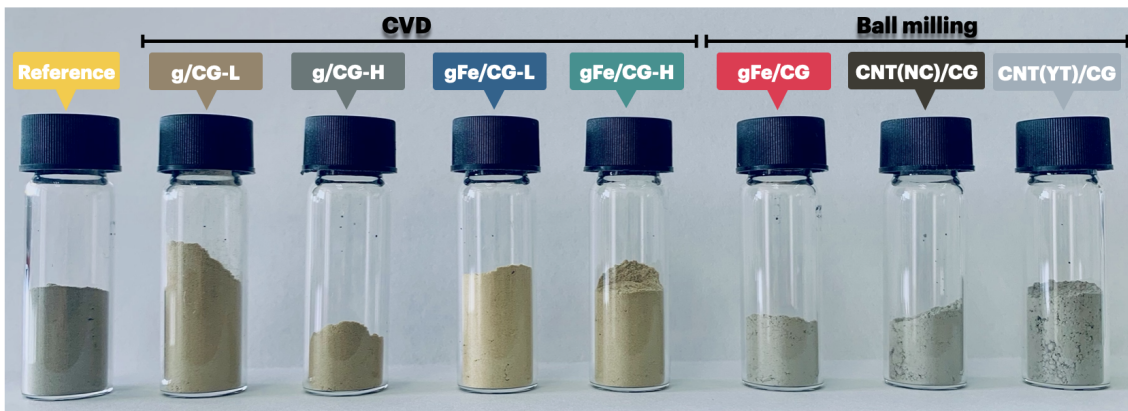


Figure 5.7: Plain cement and nano-engineered cement via CVD and Ball milling

5.2.4 XPS

Fig. 5.8a and b depict the XPS wide energy scans for plain and nano-engineered cement powders produced through CVD and ball milling, respectively. These spectra offer both qualitative and relative quantitative insights into the surface regions of the samples. Both figures show dominant elements O, Ca, C, and Si, which are characteristic of standard cement⁸⁹, along with minor surface components of Na, Mg, and P. The broad singular O 1s peaks in both figures indicate that the majority of surface oxygen exists in a similar electronic environment, or that the various oxygen signals overlap. The peak maxima, falling at 531 eV, are characteristic of silicate and carbonate oxygen⁸⁹.

Post-treatment, the C 1s spectra in Fig. 5.8a show noticeable changes, suggesting not only the presence of

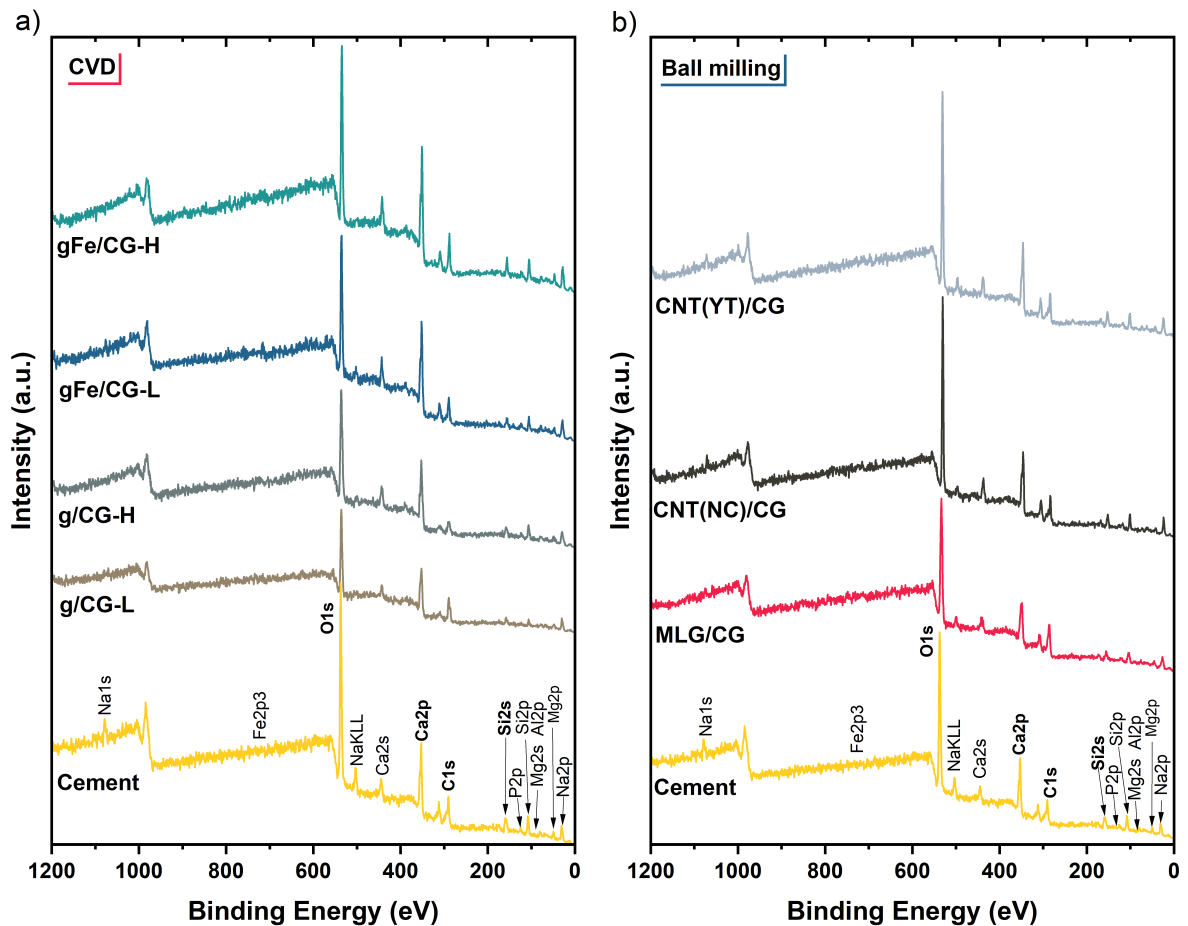


Figure 5.8: XPS patterns of plain and nano-engineered cement synthesized: a) *via* CVD, and b) through ball milling.

carbonates in the cement but also the presence of other carbon bonds such as CNS. In contrast, Fig. 5.8b shows a noticeable profile change only for MLG/CG. Another discernible change in Fig. 5.8a is the intensity of the Ca 2s peak. An increase in the intensity of the Ca 2s peak may indicate changes in the chemical or oxidation state of calcium on the cement's surface due to high-temperature treatment. As discussed in the XRD section, heating cement to high temperatures can lead to the decomposition of alite into belite and calcium oxide. This transformation involves a change in the chemical environment of Ca, potentially altering the XPS peaks associated with calcium.

Conversely, the Ca 2s and Ca 2p peaks show no significant change in Fig. 5.8b, suggesting that the intrinsic properties of the material remain unaltered.

5.2.5 Mechanical test

Sample	Compression modulus			Flexural strength		
	Mean (MPa)	SD (MPa)	%	Mean (MPa)	SD (MPa)	%
Reference	81.826	5.273	0	3.471	0.0692	0
g/CG-L	103.785	3.264	27	3.252	0.199	-6.2
g/CG-H	71.28	4.114	-12	1.738	0.271	-50
gFe/CG-L	41.14	3.335	-49	1.247	0.002	-64
gFe/CG-H	1.425	0.431	-98	0.040	0	-98
MLG/CG	118.17	4.3607	> 45	7.276	0.267	110
CNT(NC)/CG	79.558	7.783	-3	3.315	0.414	-4
CNT(YT)/CG	120.01	2.404	>45	4.147	0.149	20

Table 5.1: Compression modulus and flexural strength test results: Mean values, standard deviations, and percentage increase or decrease relative to the reference value of zero.

The results for compressive modulus and flexural strength of reference and nanocomposites after 14 days of curing are shown in table 5.1 and depicted in Fig. 5.9. Fig. 5.9a and b illustrate the procedure used to measure compressive and flexural strength with universal testing equipment. Fig. 5.9c show that the compressive modulus of *g/CG-L* increases by 27% with respect to control exhibiting 82 MPa. However, as the temperature rises, the strength of *g/CG-H* decreases by 12%. The subsequent results for *gFe/CG-L* and *gFe/CG-H* also demonstrate a similar temperature effect. Most importantly, they indicate that adding *g/FeCl₃* significantly reduces the strength, almost causing complete destruction at 1000 °C. These findings further support the notion that alite, an essential component crucial for effective cement hydration, undergoes damage as the temperature rises and iron is added, directly impacting concrete strength, as discussed in the XRD analysis.

The next set of bars displays the results obtained using ball milling. In these results, *MLG/CG* and *CNT(YT)/CG* exhibit the best outcomes, "surpassing"[†] 120 MPa (> 45%), while *CNT(CN)/CG* shows no significant change. This

[†]The equipment is only capable of measuring up to 118 MPa, thus the actual compression strength of *MLG/CG* and *CNT(YT)/CG* could not be determined.

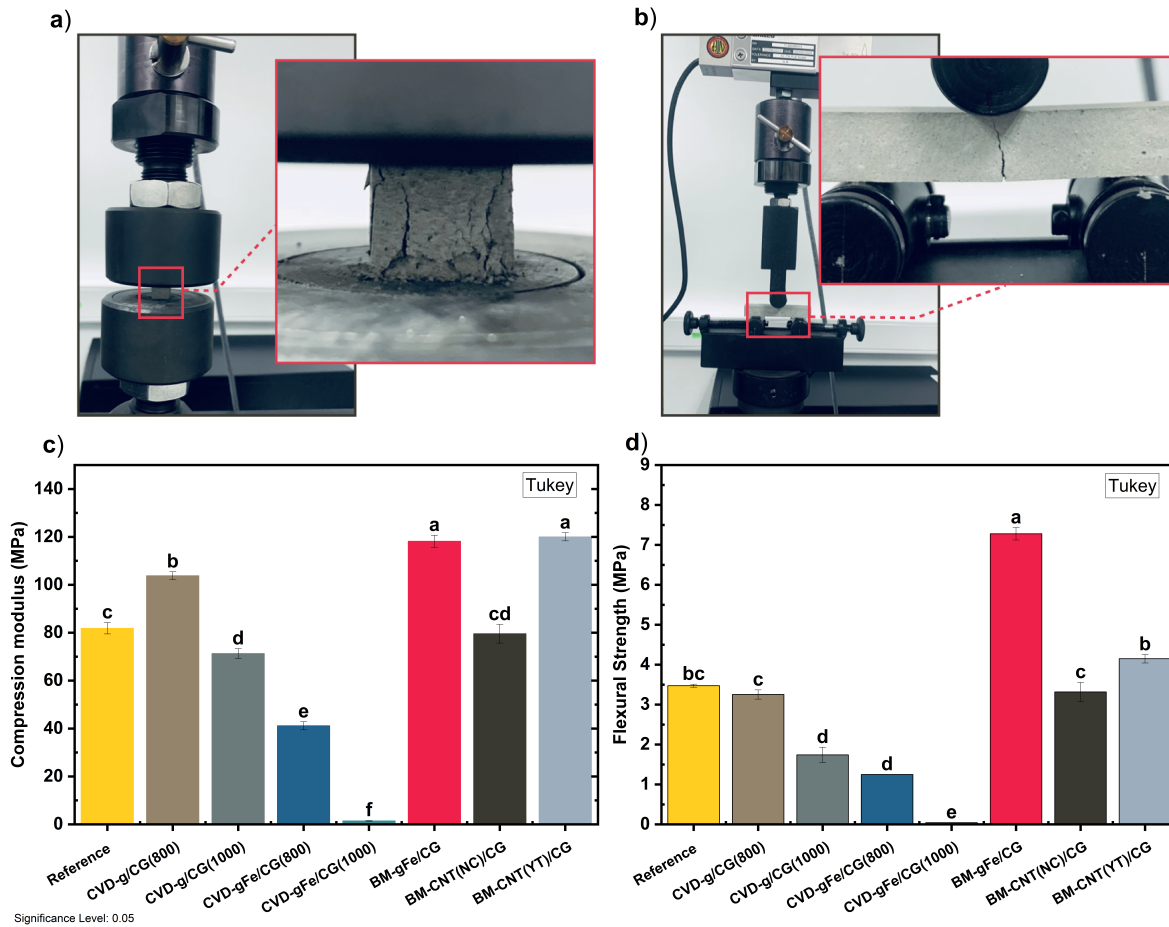


Figure 5.9: Mechanical tests: a) Compression and b) Flexural. Graphical representation illustrating the mechanical behavior of mortar prepared with plain cement and nano-engineered cement, depicting c) Compressive modulus, and d) Flexural strength.

out come is in accordance with Raman results where they show higher functionalization⁹⁰. The enhanced compressive performance can be due to the outstanding characteristics of *CNTs* and *MLG*, such as their ability to fill pores and create bridges that improve compressive strength⁹¹. It is noteworthy to mention that *CNT(YT)* were not subjected to purification, preserving their original structure and a catalyst mainly composed of carbonate. Conversely, *CNT(NC)* were previously purified, undergoing acid treatment, resulting in the loss of their end caps and breakage, as suggested by the Raman spectra in Fig. 5.3.

Moving forward with Fig. 5.9d, it is clear that there is no significant change in the flexural strength for *g/CG-L*. However, as the temperature increases and iron oxide is added, the strength of *g/CG-H*, *gFe/CG-L* and

$gFe/CG - H$ drops drastically, consistent with the compression results. In the bars representing the ball milling process, $CNT(NC)/CG$, $CNT(YT)/CG$ and MLG/CG , there is no significant change with the addition of both CNTs; however, an impressive increase of 110% is observed with MLG. This substantial improvement leads us to hypothesize that graphene flakes might be oriented perpendicular to the pressing bar, covering a larger surface area than both CNTs and leading to higher flexural strength⁹¹. Additionally, the graphene flakes may facilitate interactions from both upper and lower surfaces, enhancing interfacial interactions and subsequent bonding, as suggested by Sharma et al.⁹⁰.

5.2.6 SXISE

Following mechanical test, the remaining specimens were examined using a secondary electron detector, which was installed on XPS. We now focus on the samples that exhibited improved mechanical properties.

Figures 5.10a, b, c, and d display SXISE images of the plain mortar with scales of 100, 20, 10, and 5 μm , respectively. In Fig. 5.10a, the surface of the mortar appears powdery with looser appearance. Subsequently, in Fig. 5.10b, the mortar shows significant crystallization in an oval pattern, resembling a sponge-like structure. In Fig. 5.10c, the yellow arrows indicate cracks/fractures that occurred during the mechanical test. Finally, in the last figure, the blue arrow highlights the profile of the fracture, which appears rounded and smooth.

Fig. 5.11a, b, and c present SXISE images of nano-engineered cement, produced using $CNT(YT)$, with scales of 100, 20, and 10 μm , respectively. In Fig. 5.11a, the surface of the structure appears smooth. However, in Fig. 5.11b, a highly irregular profile is evident. Upon further magnification of these irregularities in Fig. 5.11c, tiny tubes covered by cement mortar protruding from the structure become apparent. At the fracture site, indicated by the yellow dashed line, a nanobridge is observed, attributed to the presence of CNT. Additionally, Fig. 5.11c shows yellow arrows pointing to cracks or fractures that occurred during the mechanical test.

In the last set of SXISE images, Fig. 5.12a, b, and c depict nano-engineered cement, produced using MLG, with scales of 100, 20, and 10 μm , respectively. In Fig. 5.12a, there isn't much deviation compared to the previous ones. However, in the subsequent Figure 5.12b, the surface appears to be well compacted, suggesting better hydration. The yellow arrows in the final Figure 5.12c indicate fractures suffered during the mechanical test, while the green dashed lines indicate the presence of MLG planes. In contrast to the previous composite ($CNT(YT)/CG$), MLG/CG exhibits a smooth profile.

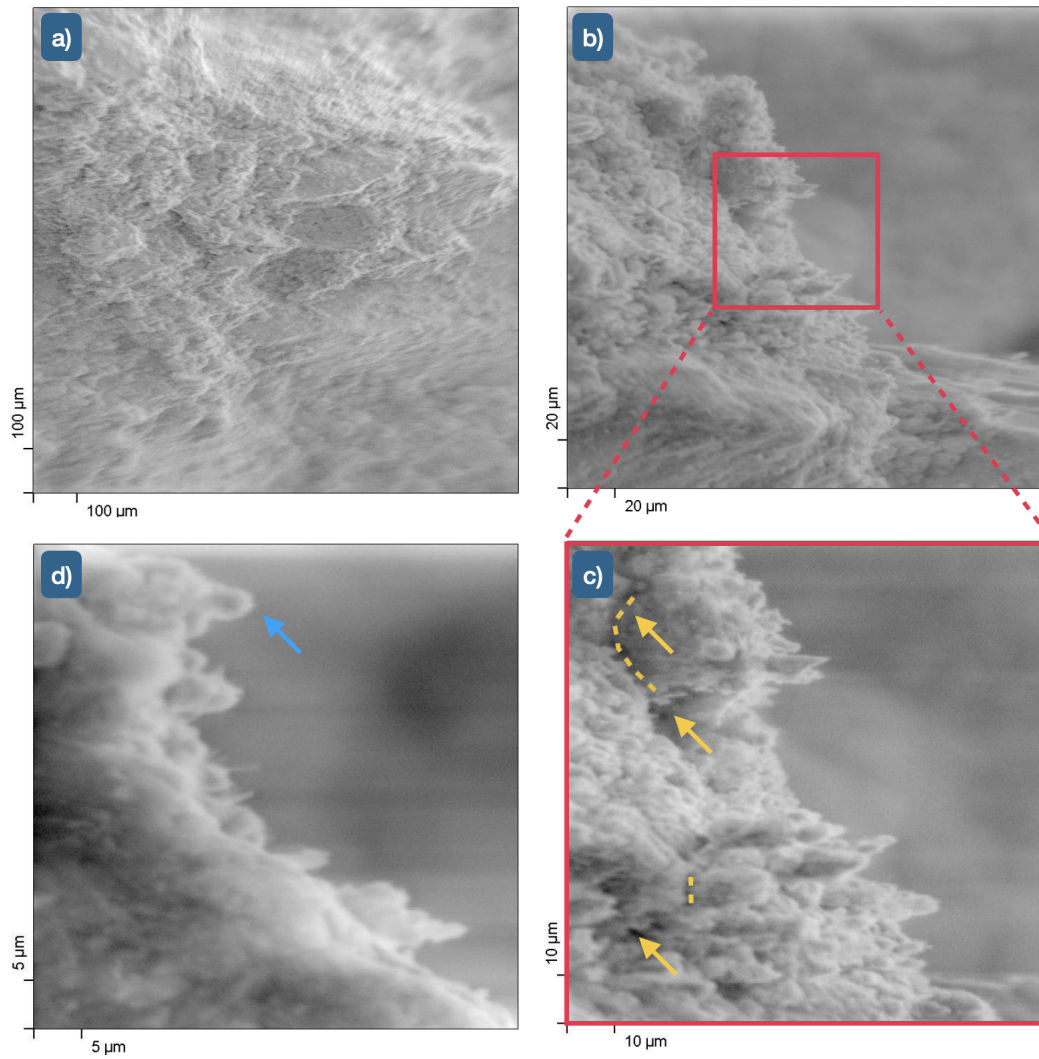


Figure 5.10: SXISE image of plain mortar with Figs. a, b, c, and d depicting scales of 100, 20, 10 and 5 μm , respectively. The yellow and blue arrows indicate the presence of fractures and the boundary shape, respectively.

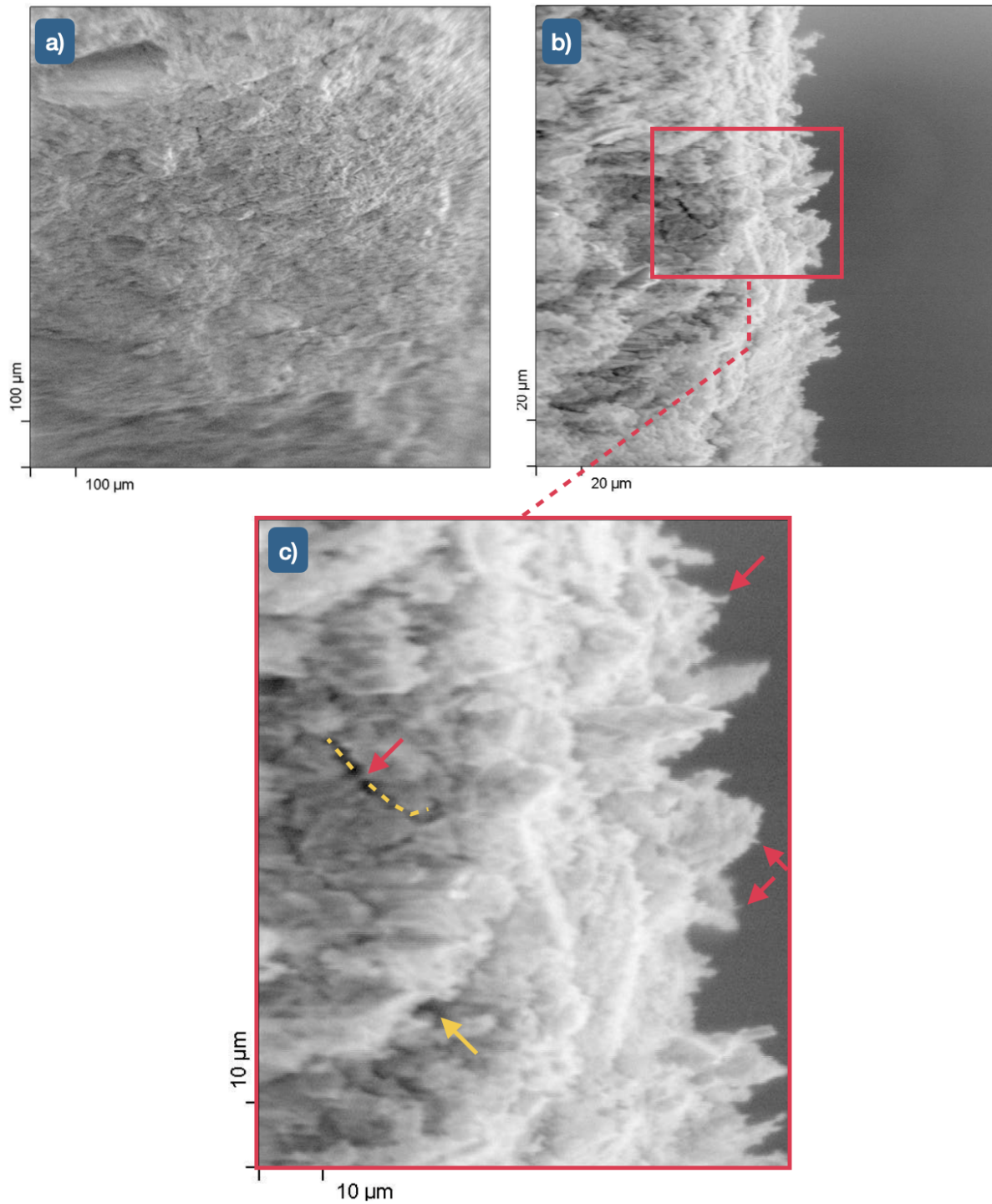


Figure 5.11: SXISE images of mortar produced using nano-engineered cement, CNT(YT)/CG. Figures a, b, and c depict scales of 100, 20, and 10 μm , respectively. The yellow dashed lines and arrows highlight the presence of fractures, while the red arrows point to the CNTs.

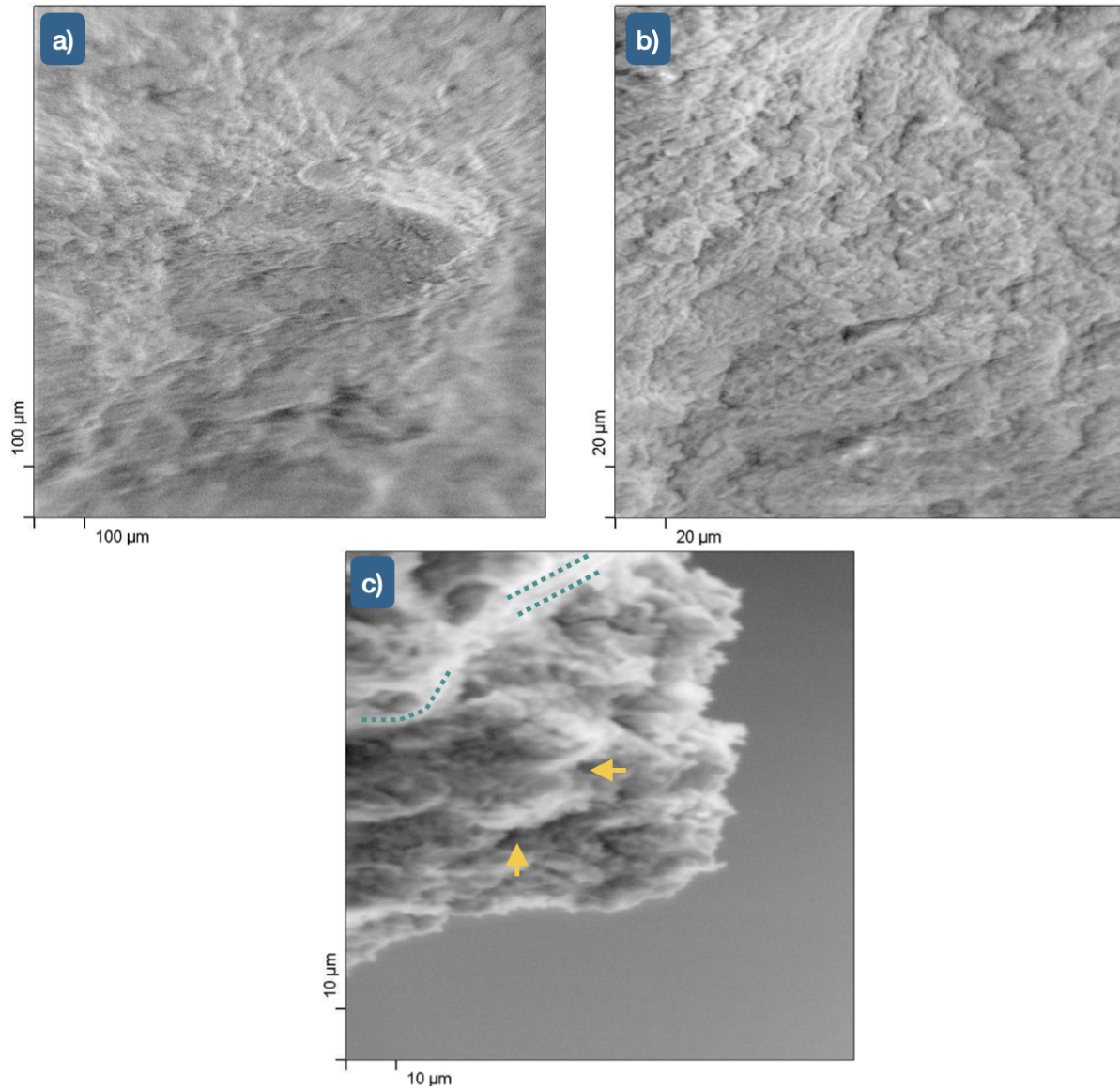


Figure 5.12: SXISE images of mortar produced with nano-engineered cement, MLG/CG, with Figs. a, b, and c depicting scales of 100, 20, and 10 μm , respectively. The yellow arrows indicate the presence of fractures, while the green dashed lines shows MLG planes.

5.2.7 Water immersion test

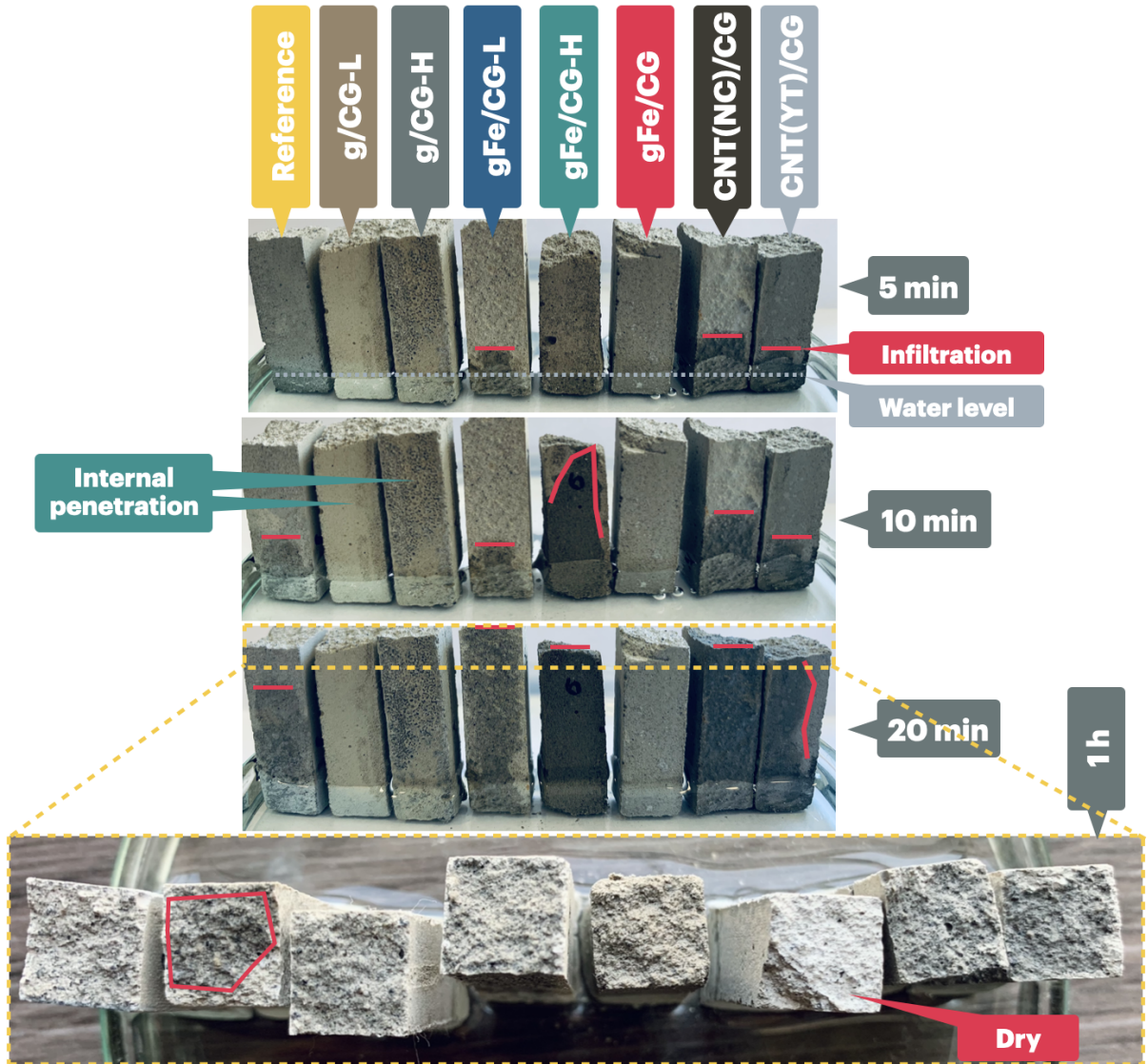


Figure 5.13: Water penetration of mortar, produced with pure cement and nano-engineered cement, tested after 28 days.

The durability of concrete is influenced by its ability to resist the penetration of fluids into its microstructure⁹². Concrete degradation processes are typically linked to the potential damage caused by water infiltration. To assess the

water immersion, specimens were immersed in water up to a specific level as shown diagrammatically in Fig. 5.13. The red lines depict the water infiltration depth into the concrete structure after 5, 10, and 30 minutes of immersion. As anticipated, in the case of the CVD sample, the water penetration in specimens prepared with nano-engineered cement follows the XRD pattern. Specifically, as the intensity of C_3S decreases in the diffractogram, the infiltration increases, with the sample synthesized at $1000\text{ }^\circ\text{C}$ and iron oxide addition exhibiting the highest infiltration. In contrast, for ball milling samples, the water penetration in samples containing CNTs remains similar to that of the reference, suggesting that the integration of CNTs has not significantly affected this property. Importantly, penetration is undetectable for the sample containing GML. After one hour, all specimens are saturated with water except for the sample containing GML.

Therefore, we hypothesize that mortar reinforced with MLG acts as a protective barrier against water penetration⁹³. The findings indicate that the increased formation of nucleation sites for $C-S-H$ hydration crystals and the large surface area of MLG create a denser network of interconnected cement crystals^{92,93}. This not only enhances the mechanical properties of concrete but also acts as a barrier against water seepage, thereby reducing the volume of water that can infiltrate through capillary pores or cracks in the concrete structure.

Chapter 6

Conclusions & Outlook

In conclusion, MLG was successfully synthesized using CVD with a mixture of glucose and iron chloride as the carbon precursor. This opened the possibility for attempting the direct incorporation of CNS into the cement matrix by blending glucose with cement and employing CVD. Raman spectroscopy results indicate the successful growth of CNS within the cement matrix, resulting in the production of nano-engineered cement. However, unfortunately, during the synthesis using this approach, one of the main cement phases, alite, undergoes thermal degradation, directly impacting the effective cement hydration.

In the second approach, utilizing ball milling, Raman spectra showed CNS vibrations alongside cement vibration modes, indicating the presence of CNS in the cement matrix. Intensity ratios and isolated optical images of CNS revealed the successful functionalization and dispersion of GML and CNT(YT) within and alongside the cement matrix. Furthermore, XRD results indicated that this approach was non-invasive, preserving the intrinsic properties of cement.

The mechanical properties exhibit a direct impact from the thermal degradation of cement. In the first approach, CVD, both compressive and flexural strength were directly affected by thermal degradation. Specifically, as the synthesis temperature increased, the mechanical properties diminished. In the second approach, as expected, the mechanical properties of cement did not undergo alteration but rather showed improvements, especially for the nanocomposite containing MLG. There was a notable increase of > 48% for compressive strength and 110% in flexural strength, surpassing common literature results. Additionally this nanocomposite shown the highest protective barrier against water penetration.

These outcomes lead us to hypothesize that graphene flakes might align perpendicular to the pressing bar, covering a larger surface area and potentially contributing to higher flexural strength. Moreover, facilitating interactions between the upper and lower surfaces may enhance interfacial connections, promoting the formation of nucleation sites for $C - S - H$ hydration crystals. The large surface area of MLG creates a denser network of interconnected cement crystals. This not only improves the mechanical properties of concrete but also acts as a barrier against water seepage. This property is crucial for ensuring the long-term durability of concrete, particularly in preventing reactions that occur in the presence of moisture, which can lead to severe cracking and critical structural problems.

Overall, the effective dispersion of CNS within the cement matrix opens up new opportunities for developing sustainable, durable structures and advanced smart materials that meet modern infrastructure needs. The scalability and cost-effectiveness of this synthesis method make it a promising approach for large-scale production and implementation, highlighting the potential of nano-engineered cement to profoundly influence the construction industry in the coming years.

Bibliography

- [1] Filippo Ubertini, Simon Laflamme, and Antonella D'Alessandro. Smart cement paste with carbon nanotubes. In *Innovative Developments of Advanced Multifunctional Nanocomposites in Civil and Structural Engineering*, pages 97–120. Elsevier, 2016.
- [2] Dong Lu and Jing Zhong. Carbon-based nanomaterials engineered cement composites: a review. *Journal of Infrastructure Preservation and Resilience*, 3(1):1–20, 2022.
- [3] Samuel Chuah, Zhu Pan, Jay G Sanjayan, Chien Ming Wang, and Wen Hui Duan. Nano reinforced cement and concrete composites and new perspective from graphene oxide. *Construction and Building materials*, 73: 113–124, 2014.
- [4] MS Konsta-Gdoutos. Nanotechnology for eco-efficient concrete. In *Eco-Efficient Concrete*, pages 544–564. Elsevier, 2013.
- [5] Natt Makul. Advanced smart concrete-a review of current progress, benefits and challenges. *Journal of Cleaner Production*, 274:122899, 2020.
- [6] Youli Lin and Hongjian Du. Graphene reinforced cement composites: A review. *Construction and Building Materials*, 265:120312, 2020.
- [7] Z Zhang, Y Yao, H Liu, Y Zhuge, and D Zhang. A new dispersion strategy to achieve high performance graphene-based cement material. In *International conference on Variability of the Sun and sun-like stars: from asteroeismology to space weather*, pages 223–232. Springer Nature Singapore Singapore, 2022.
- [8] Beate Krause, Mandy Mende, Petra Pötschke, and Gudrun Petzold. Dispersability and particle size distribution of cnts in an aqueous surfactant dispersion as a function of ultrasonic treatment time. *Carbon*, 48(10):2746–2754, 2010.
- [9] Achilleas Sesis, Mark Hodnett, Gianluca Memoli, Andrew J Wain, Izabela Jurewicz, Alan B Dalton, J David Carey, and Gareth Hinds. Influence of acoustic cavitation on the controlled ultrasonic dispersion of carbon nanotubes. *The Journal of Physical Chemistry B*, 117(48):15141–15150, 2013.

- [10] Yanfeng Jiang, Hao Song, and Rui Xu. Research on the dispersion of carbon nanotubes by ultrasonic oscillation, surfactant and centrifugation respectively and fiscal policies for its industrial development. *Ultrasonics sonochemistry*, 48:30–38, 2018.
- [11] Dan Liu, Quanfeng Huang, and Yiqin Mao. Sonication-driven dispersion of multiwalled carbon nanotubes in water with the aid of na+-montmorillonite. *Journal of Dispersion Science and Technology*, 43(4):598–604, 2022.
- [12] Waqar Ahmed, Abdelbary Elhissi, and Karthikeyan Subramani. Chapter 1 - introduction to nanotechnology. In Karthikeyan Subramani, Waqar Ahmed, and James K. Hartsfield, editors, *Nanobiomaterials in Clinical Dentistry*, pages 3–16. William Andrew Publishing, 2013.
- [13] Marcio Loos. Chapter 1 - nanoscience and nanotechnology. In Marcio Loos, editor, *Carbon Nanotube Reinforced Composites*, pages 1–36. William Andrew Publishing, Oxford, 2015.
- [14] NB Singh. Properties of cement and concrete in presence of nanomaterials. In *Smart Nanoconcretes and Cement-Based Materials*, pages 9–39. Elsevier, 2020.
- [15] RB Heimann, SE Evsukov, and Y Koga. Carbon allotropes: a suggested classification scheme based on valence orbital hybridization. *Carbon*, 35(10-11):1654–1658, 1997.
- [16] Qi-Long Yan, Michael Gozin, Feng-Qi Zhao, Adva Cohen, and Si-Ping Pang. Highly energetic compositions based on functionalized carbon nanomaterials. *Nanoscale*, 8(9):4799–4851, 2016.
- [17] U Naresh, N Suresh Kumar, D Baba Basha, Prasun Benerjee, K Chandra Babu Naidu, R Jeevan Kumar, Ramyakrishna Pothu, and Rajender Boddula. Synthesis and properties of graphene-based materials. *Monoelements: Properties and Applications*, pages 57–72, 2020.
- [18] Michio Inagaki, Feiyu Kang, Masahiro Toyoda, and Hidetaka Konno. Chapter 3 - graphene: Synthesis and preparation. In Michio Inagaki, Feiyu Kang, Masahiro Toyoda, and Hidetaka Konno, editors, *Advanced Materials Science and Engineering of Carbon*, pages 41–65. Butterworth-Heinemann, Boston, 2014.
- [19] Zhiping Xu. 4 - fundamental properties of graphene. In Hongwei Zhu, Zhiping Xu, Dan Xie, and Ying Fang, editors, *Graphene*, pages 73–102. Academic Press, 2018.
- [20] Boris Ildusovich Kharisov and Oxana Vasilievna Kharissova. *Classic Carbon Nanostructures*, pages 35–109. Springer International Publishing, Cham, 2019.
- [21] Paul Bazylewski and Giovanni Fanchini. 1.13 - graphene: Properties and applications. In David L. Andrews, Robert H. Lipson, and Thomas Nann, editors, *Comprehensive Nanoscience and Nanotechnology (Second Edition)*, pages 287–304. Academic Press, Oxford, second edition edition, 2019.
- [22] Nikhil A Koratkar. *Graphene in composite materials: Synthesis, characterization and applications*. DEStech Publications, Inc, 2013.

- [23] Ed Gerstner. Nobel prize 2010: Andre geim & konstantin novoselov. *Nature Physics*, 6(11):836–836, 2010.
- [24] Yong Seok Choi, Je Min Yoo, and Byung Hee Hong. 2 - structure and properties of graphene. In Tae-Woo Lee, editor, *Graphene for Flexible Lighting and Displays*, Woodhead Publishing Series in Electronic and Optical Materials, pages 5–26. Woodhead Publishing, 2020.
- [25] Boris Ildusovich Kharisov and Oxana Vasilievna Kharissova. *Carbon allotropes: metal-complex chemistry, properties and applications*. Springer, 2019.
- [26] A. H. Castro Neto, F. Guinea, N. M. R. Peres, K. S. Novoselov, and A. K. Geim. The electronic properties of graphene. *Rev. Mod. Phys.*, 81:109–162, Jan 2009. doi: 10.1103/RevModPhys.81.109. URL <https://link.aps.org/doi/10.1103/RevModPhys.81.109>.
- [27] Dimitrios G. Papageorgiou, Ian A. Kinloch, and Robert J. Young. Mechanical properties of graphene and graphene-based nanocomposites. *Progress in Materials Science*, 90:75–127, 2017.
- [28] Changgu Lee, Xiaoding Wei, Jeffrey W Kysar, and James Hone. Measurement of the elastic properties and intrinsic strength of monolayer graphene. *science*, 321(5887):385–388, 2008.
- [29] Sumio Iijima. Helical microtubules of graphitic carbon. *nature*, 354(6348):56–58, 1991.
- [30] Marcio Loos. Chapter 3 - allotropes of carbon and carbon nanotubes. In Marcio Loos, editor, *Carbon Nanotube Reinforced Composites*, pages 73–101. William Andrew Publishing, Oxford, 2015.
- [31] Abd El-Moez A. Mohamed and Mohamed A. Mohamed. Carbon Nanomaterials for Agri-Food and Environmental Applications. (*ACS Nano* 10 2016):21–32, 2020. doi: 10.1016/b978-0-12-819786-8.00002-5.
- [32] Ghanshyam Pal and Shanmugam Kumar. Mechanical properties of isolated carbon nanotube. In *Carbon Nanotube-Reinforced Polymers*, pages 173–199. Elsevier, 2018.
- [33] Boris Ildusovich Kharisov and Oxana Vasilievna Kharissova. *Carbon Allotropes: Metal-Complex Chemistry, Properties and Applications*. 2019.
- [34] H. Qiu and J. Yang. *Industrial Applications of Carbon Nanotubes*. pages 47–69, 2017.
- [35] Jose Martin Herrera-Ramirez, Raul Perez-Bustamante, and Alfredo Aguilar-Elguezabal. An overview of the synthesis, characterization, and applications of carbon nanotubes. *Carbon-Based Nanofillers and Their Rubber Nanocomposites*, pages 47–75, 2019.
- [36] Mehran Tehrani and Pouria Khanbolouki. Carbon nanotubes: synthesis, characterization, and applications. *Advances in Nanomaterials: Fundamentals, Properties and Applications*, pages 3–35, 2018.
- [37] Ferial Ghaemi, May Ali, Robiah Yunus, and Raja Nor Othman. Synthesis of carbon nanomaterials using catalytic chemical vapor deposition technique. In *Synthesis, technology and applications of carbon nanomaterials*, pages 1–27. Elsevier, 2019.

- [38] Harry FW Taylor et al. *Cement chemistry*, volume 2. Thomas Telford London, 1997.
- [39] P.-C. Aïtcin. 3 - portland cement. In Pierre-Claude Aïtcin and Robert J Flatt, editors, *Science and Technology of Concrete Admixtures*, pages 27–51. Woodhead Publishing, 2016.
- [40] Pierre-Claude Aïtcin. *Binders for durable and sustainable concrete*. CRC Press, 2007.
- [41] Peter Hewlett and Martin Liska. *Lea's chemistry of cement and concrete*. Butterworth-Heinemann, 2019.
- [42] Jeffrey W Bullard, Hamlin M Jennings, Richard A Livingston, Andre Nonat, George W Scherer, Jeffrey S Schweitzer, Karen L Scrivener, and Jeffrey J Thomas. Mechanisms of cement hydration. *Cement and concrete research*, 41(12):1208–1223, 2011.
- [43] D Marchon and Robert J Flatt. Mechanisms of cement hydration. In *Science and technology of concrete admixtures*, pages 129–145. Elsevier, 2016.
- [44] Farzad Ebrahimi and Ali Dabbagh. 1 - introduction to composites, nanocomposites, and hybrid nanocomposites. In Farzad Ebrahimi and Ali Dabbagh, editors, *Mechanics of Multiscale Hybrid Nanocomposites*, pages 1–80. Elsevier, 2022.
- [45] Pedro Henrique Cury Camargo, Kestur Gundappa Satyanarayana, and Fernando Wypych. Nanocomposites: synthesis, structure, properties and new application opportunities. *Materials Research*, 12:1–39, 2009.
- [46] Manab Mallik and Mainak Saha. Carbon-based nanocomposites: Processing, electronic properties and applications. In *Carbon Nanomaterial Electronics: Devices and Applications*, pages 97–122. Springer, 2021.
- [47] Nabeel Hasan Al-Mutairi, Atheer Hussain Mehdi, and Ban Jawad Kadhim. Nanocomposites materials definitions, types and some of their applications: A review. *European Journal of Research Development and Sustainability*, 3(2):102–108, 2022.
- [48] T. James. Global breakthrough: Graphene-infused concrete conducts electricity, Sep 2018. URL <https://www.internationales-verkehrswesen.de/concrete-conducts-electricity/>.
- [49] Reginald Davey. Creating smart cement with graphene-coated sand, Jul 2022. URL <https://www.azom.com/news.aspx?newsID=59594>.
- [50] Kai Cui, Jun Chang, Luciano Feo, Cheuk Lun Chow, and Denvi Lau. Developments and applications of carbon nanotube reinforced cement-based composites as functional building materials. *Frontiers in Materials*, 9, 2022.
- [51] NB Singh. Properties of cement and concrete in presence of nanomaterials. In *Smart Nanoconcretes and Cement-Based Materials*, pages 9–39. Elsevier, 2020.

- [52] Dubey Rama, Dutta Dhiraj, Sarkar Arpan, and Pronobesh Chattopadhyay. Functionalized carbon nanotubes: synthesis, properties and applications in water purification, drug delivery, and material and biomedical sciences. *Nanoscale Adv.*, 3:5722–5744, 2021.
- [53] Abhijit Biswas, Tao Wang, and Alexandru S Biris. Single metal nanoparticle spectroscopy: optical characterization of individual nanosystems for biomedical applications. *Nanoscale*, 2(9):1560–1572, 2010.
- [54] Bhim Prasad Kafle. Chapter 8 - raman spectroscopy. In Bhim Prasad Kafle, editor, *Chemical Analysis and Material Characterization by Spectrophotometry*, pages 245–268. Elsevier, 2020.
- [55] Nebu John and Sony George. Chapter 5 - raman spectroscopy. In Sabu Thomas, Raju Thomas, Ajesh K. Zachariah, and Raghvendra Kumar Mishra, editors, *Spectroscopic Methods for Nanomaterials Characterization*, Micro and Nano Technologies, pages 95–127. Elsevier, 2017.
- [56] Padmnabh Rai and Satish Kumar Dubey. *Raman Spectroscopy: A Potential Characterization Tool for Carbon Materials*, pages 405–434. Springer International Publishing, Cham, 2018.
- [57] Mirosław Szybowicz, Ariadna B. Nowicka, and Anna Dychalska. Chapter 1 - characterization of carbon nanomaterials by raman spectroscopy. In Sneha Mohan Bhagyaraj, Oluwatobi Samuel Oluwafemi, Nandakumar Kalarikkal, and Sabu Thomas, editors, *Characterization of Nanomaterials*, Micro and Nano Technologies, pages 1–36. Woodhead Publishing, 2018.
- [58] Andrea C Ferrari and Denis M Basko. Raman spectroscopy as a versatile tool for studying the properties of graphene. *Nature nanotechnology*, 8(4):235–246, 2013.
- [59] Jiang-Bin Wu, Miao-Ling Lin, Xin Cong, He-Nan Liu, and Ping-Heng Tan. Raman spectroscopy of graphene-based materials and its applications in related devices. *Chemical Society Reviews*, 47(5):1822–1873, 2018.
- [60] Zheling Li, Libo Deng, Ian A. Kinloch, and Robert J. Young. Raman spectroscopy of carbon materials and their composites: Graphene, nanotubes and fibres. *Progress in Materials Science*, 135:101089, 2023.
- [61] Maria Kaliva and Maria Vamvakaki. Chapter 17 - nanomaterials characterization. In Ravin Narain, editor, *Polymer Science and Nanotechnology*, pages 401–433. Elsevier, 2020.
- [62] Wikipedia contributors. Photoemission spectroscopy — Wikipedia, the free encyclopedia, 2023. URL https://en.wikipedia.org/w/index.php?title=Photoemission_spectroscopy&oldid=1189273781. [Online; accessed 2-February-2024].
- [63] M. Aziz and A.F. Ismail. Chapter 5 - x-ray photoelectron spectroscopy (xps). In Nidal Hilal, Ahmad Fauzi Ismail, Takeshi Matsuura, and Darren Oatley-Radcliffe, editors, *Membrane Characterization*, pages 81–93. Elsevier, 2017.
- [64] D. Nanda Gopala Krishna and John Philip. Review on surface-characterization applications of x-ray photoelectron spectroscopy (xps): Recent developments and challenges. *Applied Surface Science Advances*, 12:100332, 2022.

- [65] Scanning electron microscopy. URL https://myscope.training/#/SEMlevel_3_1.
- [66] Author Name. Physical electronics, Year Published. URL <https://www.phy.com/index.html>. February 7, 2024.
- [67] Sravanthi Loganathan, Ravi Babu Valapa, Raghvendra Kumar Mishra, G. Pugazhenthii, and Sabu Thomas. Chapter 4 - thermogravimetric analysis for characterization of nanomaterials. In Sabu Thomas, Raju Thomas, Ajesh K. Zachariah, and Raghvendra Kumar Mishra, editors, *Thermal and Rheological Measurement Techniques for Nanomaterials Characterization*, Micro and Nano Technologies, pages 67–108. Elsevier, 2017. ISBN 978-0-323-46139-9. doi: <https://doi.org/10.1016/B978-0-323-46139-9.00004-9>. URL <https://www.sciencedirect.com/science/article/pii/B9780323461399000049>.
- [68] Stanley R. Sandler, Wolf Karo, Jo-Anne Bonesteel, and Eli M. Pearce. Experiment 15 - thermogravimetric analysis. In Stanley R. Sandler, Wolf Karo, Jo-Anne Bonesteel, and Eli M. Pearce, editors, *Polymer Synthesis and Characterization*, pages 108–119. Academic Press, San Diego, 1998. ISBN 978-0-12-618240-8. doi: <https://doi.org/10.1016/B978-012618240-8/50022-8>. URL <https://www.sciencedirect.com/science/article/pii/B9780126182408500228>.
- [69] S Mahmood Fatemi and Masumeh Foroutan. Recent developments concerning the dispersion of carbon nanotubes in surfactant/polymer systems by md simulation. *Journal of Nanostructure in Chemistry*, 6:29–40, 2016.
- [70] Binbin Zhang, Jinliang Song, Guanying Yang, and Buxing Han. Large-scale production of high-quality graphene using glucose and ferric chloride. *Chemical Science*, 5(12):4656–4660, 2014.
- [71] Marco Liebscher, Lazaros Tzounis, Dominik Junger, Tin Trong Dinh, and Viktor Mechtcherine. Electrical joule heating of cementitious nanocomposites filled with multi-walled carbon nanotubes: role of filler concentration, water content, and cement age. *Smart Materials and Structures*, 29(12):125019, nov 2020.
- [72] Xun Zhang, Sheng Chen, Shri Ramaswamy, Yoon Soo Kim, and Feng Xu. Obtaining pure spectra of hemi-cellulose and cellulose from poplar cell wall Raman imaging data. *Cellulose*, 24(11):4671–4682, 2017. ISSN 0969-0239. doi: [10.1007/s10570-017-1486-4](https://doi.org/10.1007/s10570-017-1486-4).
- [73] A. C. Ferrari and J. Robertson. Interpretation of Raman spectra of disordered and amorphous carbon. *Physical Review B*, 61(20):14095–14107, 2000. ISSN 1098-0121. doi: [10.1103/physrevb.61.14095](https://doi.org/10.1103/physrevb.61.14095).
- [74] Avery B. Brown, Geoffrey A. Tompsett, Behnam Partopour, N. Aaron Deskins, and Michael T. Timko. Hydrochar structural determination from artifact-free Raman analysis. *Carbon*, 167:378–387, 2020. ISSN 0008-6223. doi: [10.1016/j.carbon.2020.06.021](https://doi.org/10.1016/j.carbon.2020.06.021). Raman, Mechanism.
- [75] Marta Sevilla and Antonio B. Fuertes. Chemical and Structural Properties of Carbonaceous Products Obtained by Hydrothermal Carbonization of Saccharides. *Chemistry – A European Journal*, 15(16):4195–4203, 2009. ISSN 0947-6539. doi: [10.1002/chem.200802097](https://doi.org/10.1002/chem.200802097).

- [76] Xiaofeng Liu, Cristina Giordano, and Markus Antonietti. A Facile Molten-Salt Route to Graphene Synthesis. *Small*, 10(1):193–200, 2014. ISSN 1613-6810. doi: 10.1002/sml.201300812.
- [77] Dongshuai Hou, Zeyu Lu, Xiangyu Li, Hongyan Ma, and Zongjin Li. Reactive molecular dynamics and experimental study of graphene-cement composites: Structure, dynamics and reinforcement mechanisms. *Carbon*, 115:188–208, 2017.
- [78] Yao Yao, Zhenyu Zhang, Hu Liu, Yan Zhuge, and Dong Zhang. A new in-situ growth strategy to achieve high performance graphene-based cement material. *Construction and Building Materials*, 335:127451, 2022.
- [79] M Galimberti. Advances in ordinary portland cement clinker: Reducing the environmental impact of the production process. 2017. URL <https://api.semanticscholar.org/CorpusID:114527339>.
- [80] Rohan Jadhav and NC Debnath. Computation of x-ray powder diffractograms of cement components and its application to phase analysis and hydration performance of opc cement. *Bulletin of Materials Science*, 34(5): 1137–1150, 2011.
- [81] ET Carlson. The decomposition of tricalcium silicate in the temperature range 1000–1300° c. *Bur. Standards J. Research*, 7(5):893–902, 1931.
- [82] Katharina Schraut, Florian Kargl, Christian Adam, and Oleh Ivashko. In situ synchrotron xrd measurements during solidification of a melt in the cao–sio₂ system using an aerodynamic levitation system. *Journal of Physics: Condensed Matter*, 33(26):264003, 2021.
- [83] Jorge Alberto Soares Tenório, Sérgio Sônego Raymundo Pereira, Andréa Vidal Ferreira, Denise Croce Romano Espinosa, and Fernando Gabriel da Silva Araújo. Cct diagrams of tricalcium silicate: Part i. influence of the fe₂o₃ content. *Materials Research Bulletin*, 40(3):433–438, 2005.
- [84] Gen Li and LW Zhang. Microstructure and phase transformation of graphene-cement composites under high temperature. *Composites Part B: Engineering*, 166:86–94, 2019.
- [85] Seungyeon Han, Mohammad Shakhawat Hossain, Taeho Ha, and Kyong Ku Yun. Graphene-oxide-reinforced cement composites mechanical and microstructural characteristics at elevated temperatures. *Nanotechnology Reviews*, 11(1):3174–3194, 2022.
- [86] Roman Gabrovšek, Tomaž Vuk, and Venčeslav Kaučič. Evaluation of the hydration of portland cement containing various carbonates by means of thermal analysis. *Acta Chim. Slov*, 53(2):159–165, 2006.
- [87] Harish Kumar Choudhary, AV Anupama, R Kumar, ME Panzi, S Matteppanavar, Baburao N Sherikar, and B Sahoo. Observation of phase transformations in cement during hydration. *Construction and Building Materials*, 101:122–129, 2015.
- [88] Izabela Hager. Colour change in heated concrete. *Fire Technology*, 50:945–958, 2014.

-
- [89] DAVID L COCKE, HYLTON G McWHINNEY, D CARL DUFNER, BEN HORRELL, and J Dale Ortego. An xps and eds investigation of portland cement doped with pb2+ and cr3+ cations. *Hazardous waste and hazardous materials*, 6(3):251–267, 1989.
- [90] Snigdha Sharma, NC Kothiyal, and Mani Chitkara. Enhanced mechanical performance of cement nanocomposite reinforced with graphene oxide synthesized from mechanically milled graphite and its comparison with carbon nanotubes reinforced nanocomposite. *RSC advances*, 6(106):103993–104009, 2016.
- [91] Yuhang Du, Jian Yang, Blessen Skariah Thomas, Lihui Li, Huanyu Li, and Sohaib Nazar. Hybrid graphene oxide/carbon nanotubes reinforced cement paste: An investigation on hybrid ratio. *Construction and Building Materials*, 261:119815, 2020.
- [92] Dimitar Dimov, Iddo Amit, Olivier Gorrie, Matthew D Barnes, Nicola J Townsend, Ana IS Neves, Freddie Withers, Saverio Russo, and Monica Felicia Craciun. Ultrahigh performance nanoengineered graphene–concrete composites for multifunctional applications. *Advanced functional materials*, 28(23):1705183, 2018.
- [93] Hongjian Du and Sze Dai Pang. Enhancement of barrier properties of cement mortar with graphene nanoplatelet. *Cement and Concrete Research*, 76:10–19, 2015.